WELLBORE AND NEAR-WELLBORE HEAT TRANSFER: GENERAL THEORY AND PRACTICAL APPLICATION

A Dissertation

by

MINSOO JANG

Submitted to the Graduate and Professional School of
Texas A&M University
in partial fulfillment of the requirements for the degree of

DOCTOR OF PHILOSOPHY

Chair of Committee,	A. Rashid Hasan
Co-Chair of Committee,	Nobuo Morita
Committee Members,	Hadi Nasrabadi
	Ahmad Hilaly
Head of Department,	Jeff B. Spath

December 2021

Major Subject: Petroleum Engineering

ABSTRACT

The development and production of underground hydrocarbon resources are affected by heat transfer between the fluid, downhole tubulars, and the surrounding formation. Understanding heat transfer becomes increasingly more critical in environmentally challenging reservoirs. The "rule-of-thumb" practice and complicated numerical simulations are neither reliable nor practical.

This thesis addresses analytical models for computing the wellbore or formation temperature profiles during drilling, completion, and production periods. It includes four parts: (1) the temperature profile in the counter-current flow system, (2) near-wellbore cooling effect due to drilling circulation, (3) fluid behavior identification during the clean-up period, and (4) non-isothermal fluid behavior during production.

The counter-current heat transfer model provides the temperature profiles in tubing and annulus at a minimal computational cost, a feature not available with numerical simulations. It is particularly advantageous in heavy oil wells where viscosity control is essential for flow assurance issues.

The near-wellbore cooling effect during drilling circulation may impair the reliability of applications using the measured formation temperature. This quantitative analysis provides information on the magnitude and duration of the cooling effect, reducing the uncertainty of the measured temperature.

Advanced temperature measuring device provides the ability to estimate the economic feasibility of a reservoir by using the temperature profile. Identifying the fluid behavior, interfaces, and properties - applications that were not available with the current measuring standards are introduced.

Contrary to the common assumption, the flowing fluid temperature in the reservoir is not isothermal due to several heat generation/transfer effects. A steady-state reservoir heat transfer model leads to better estimates of well productivity index, one of the key parameters in production optimization. All analytical models in this study with realistic assumptions allow engineers to estimate the temperature at a competitive computational cost.

DEDICATION

I dedicate this thesis to my family for nursing me with affections and love and their dedicated partnership for success in my life.

ACKNOWLEDGEMENTS

Throughout the writing of this dissertation, I have received a great deal of support and assistance. I would first like to thank my supervisor, Professor Abu Rashid Hasan, whose expertise was invaluable in formulating the research questions and methodology. His timely advice, meticulous scrutiny, knowledgeable advice, and scientific approach have immensely helped me accomplish this task. Without his guidance and patience, this work would never be fulfilled. His insightful feedback pushed me to sharpen my thinking and brought my work to a higher level.

I owe a deep sense of gratitude to Dr. Nobuo Morita for his keen interest in me at every stage of my research. His prompt inspirations, timely suggestions with enthusiasm, warm-hearted emotional support have enabled me to complete this dissertation.

I especially wish to thank Dr. Hadi Nasrabadi and Dr. Ahmed Hilaly for agreeing to serve on my committee. Their valuable guidance throughout my studies. They provided me with the tools needed to choose the right direction and complete my dissertation.

Besides, I would like to thank my family for their wise counsel and sympathetic ear. You are always there for me. Finally, I could not have completed this dissertation without the support of my friends, Troy Chun, Jaewoo An, and Dr. Sukgu Jeon, who provided stimulating discussions as well as happy distractions to rest my mind outside of my research.

NOMENCLATURE

A	pipe area, ft^2
B_o	oil-formation volume factor, RB/STB
B_g	gas formation volume factor, Mscf/STB
c_p	specific heat capacity, Btu/lb_m-°F
C_{JT}	Joule-Thomson coefficient, °F/ft
d	diameter, ft
f	friction factor, dimensionless
g	gravitational acceleration, ft s^{-2}
g_c	conversion factor, 32.17 $(lb_m$-ft)/lbf-s^2
g_G	surrounding temperature gradient, °F/psi
h	formation thickness, ft
h_c	heat transfer coefficient of the reservoir, Btu/hr.ft^2.°F
h_f	convective heat-transfer coefficient, Btu/hr.ft^2.°F
H	enthalpy, BTU/lbm
$\dot{Q}$	heat transfer rate with over- and under-, Btu/hr/ ft^2
J	conversion factor, 778 (ft-lbf)/Btu
k	reservoir permeability, md
K	thermal conductivity, Btu/(hr.ft.°F)
L_R	relaxation parameter, hr^{-1}
$\dot{m}$	mass flow rate, Kg/s
P	pressure, psi

P_r	Prandtl number, dimensionless
q	volumetric flow rate, ft^3/hr
Q	heat flow rate, Btu/hr
Q_F	heat flow between formation and wellbore, Btu/hr
Q_{ta}	heat flow between tubing and annulus, Btu/hr
r	radius, ft
r_d	dimensionless radius, dimensionless
r_a	affected formation radius, ft
r_e	external reservoir radius, ft
R_e	Reynolds number, dimensionless
t_{circ}	circulation time, hr
s_f	reservoir fluid saturation, dimensionless
S	saturation, dimensionless
t	time, hr
t_D	dimensionless time, dimensionless
T	temperature, °F
T_a	annulus fluid temperature, °F
T_{abh}	annulus fluid temperature at the bottom-hole, °F
T_{awh}	annulus fluid temperature at the wellhead, °F
T_D	dimensionless temperature, dimensionless
T_{ei}	undisturbed formation temperature, °F
T_{eibh}	undisturbed formation temperature at the bottom-hole, °F
T_{eiwh}	undisturbed formation temperature at the wellhead, °F

T_{inj}	injecting/inlet temperature, °F
T_t	tubing fluid temperature, °F
T_{tbh}	tubing fluid temperature at the bottom-hole, °F
T_{twh}	tubing fluid temperature at the wellhead, °F
TVD	True Vertical Depth, ft
u	fluid velocity, ft/hr
U	overall heat-transfer coefficient, Btu/hr.ft^2.°F
V	specific volume, ft3/lb_m
w	mass flow rate, lb_m/hr
z	wellbore depth, ft
Z	gas compressibility factor, dimensionless
α	thermal diffusivity, ft^2/hr
μ	viscosity, cp
ϕ	formation porosity, dimensionless
ρ	density, lb_m/ft^3
σ	fluid Joule-Thomson throttling coefficient, Btu/lb_m-psi
ε	pipe absolute roughness, ft

Subscripts

a	annulus
avg	average
bh	bottom-hole
cem	cement

ci	casing inside
circ	circulation
co	casing outside
csg	casing
e	formation
F	formation
g	gas
inj	injecting
ID	inside diameter
L	measured depth of the wellbore
o	oil
OD	outside diameter
prod	producing
t	tubing
ti	tubing inside
to	tubing outside
w	wellbore formation interface
wh	wellhead

TABLE OF CONTENTS

Page

LIST OF FIGURES

Page

LIST OF TABLES

Page

1. INTRODUCTION

1.1 Background

As the development of conventional oil and gas resources (easy oil) approaches its peak, the focus has shifted toward other unconventional resources, such as deep-sea, heavy oil, and shale with low permeability tight reservoirs. Figure 1 shows the oil production potential of North America up to the year 2030 when unconventional reservoirs are to account for more than half of the total amount (EIA, 2019). These reservoirs have challenging environments, including high pressures and temperatures, large temperature differentials, and extremely high viscosities. Thus, developing harsh environmental reservoirs requires special operations and a systematic plan.

Consideration of pressure is often reliable with a reasonable degree of accuracy for safe and efficient operation designs. In contrast, the temperature often lacks synergy with pressure due to insufficient knowledge of heat transfer and/or limitation of measuring devices. A better understanding of heat transfer can fill the gap between the required technologies to develop reservoirs in harsh environments and the current operational capacity. This thesis offers modeling and analyses of some of those heat transfer situations.

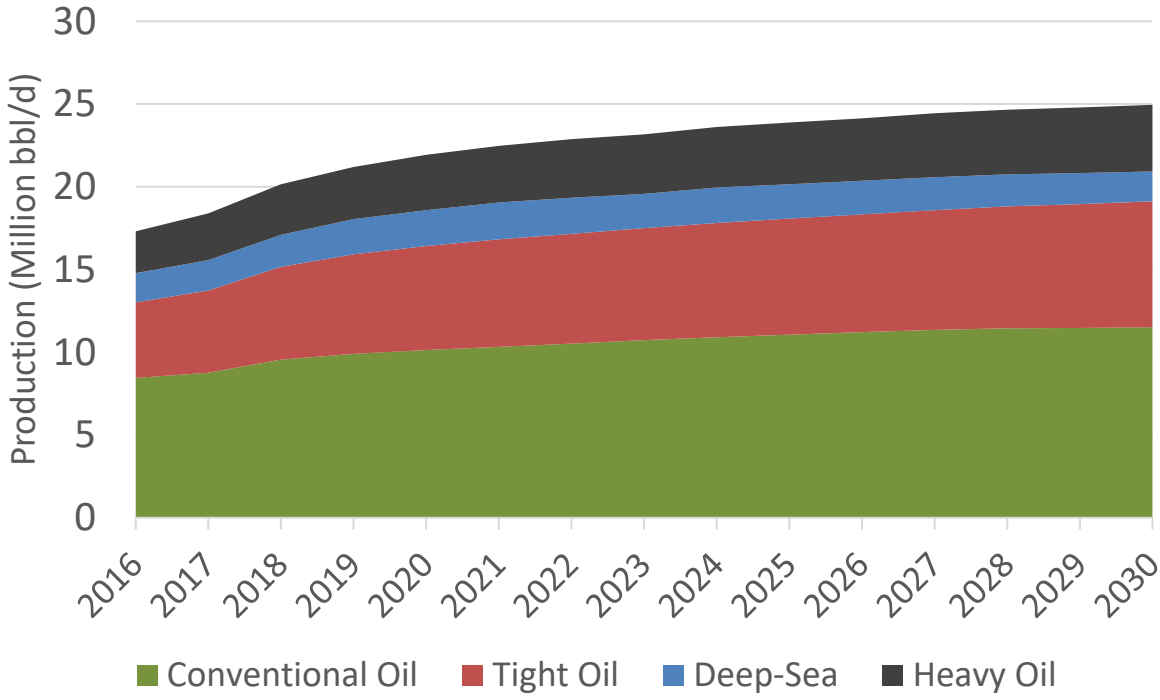

Figure 1- North American oil production potential.

1.2 Statement of the problem

The development of more challenging reservoirs, such as deep/tight oil and gas from unconventional resources, has increased dramatically in both onshore and offshore environments. Typically, unconventional reservoirs require an artificial-lift system due to rapid pressure decline or flow-ability/flow-assurance issues. Tubings are run through the casing during the artificial-lift system installation, sometimes leading to two conduits for flowing fluids. The fluid is injected into either the tubing or the annulus at the wellhead and reaches the bottom-hole. It mixes with the reservoir fluid and rises through other conduits. This counter-current flow in the tubing-annulus system adds complexity to the heat transfer process, and empirical values or complicated numerical simulations are neither reliable nor practical. Temperature estimation in the double-

conduits becomes crucial for heavy oil production. Heavy oil is a mixture of complex-structured hydrocarbons, which has a non-linear relationship between temperature and viscosity. Failure to estimate the temperature-dependent viscosity accurately leads to flow assurance issues due to inadequate design of injecting fluids and wellhead facilities. The analytical model presented in this thesis for the counter-current flow system allows field engineers to estimate temperatures for safe and cost-effective production designs with a minimal computational cost.

Heat transfer between the wellbore and the formation alters the near-wellbore formation temperature during drilling. When the cold drilling fluid is injected at the surface, the near-wellbore temperature profile down to intermediate depths is not significantly affected; however, at deeper depths (>3,000 ft), where the target perforation zones are located, the cooling effect is immense. This is because the formation temperature rises with depth, and the temperature difference between the formation and the drilling fluid increases accordingly. The warmer reservoir fluid flows through the cooled near-wellbore formation after perforation and enters into the wellbore. The near-wellbore formation is gradually heated as the warmer reservoir fluid keeps flowing and eventually converges to the undisturbed formation temperature. However, quite a long duration is required for recovering the undisturbed formation temperature due to the low thermal diffusivity value of the formation. The temperature difference between the wellbore and formation at the pay-zone decreases the temperature measurement accuracy in the drill stem test (DST). Inaccurate data can make further applications useless, such as rate estimation and subsequent zonal allocation techniques. Therefore, quantitative assessment of the near-wellbore cooling effect is necessary for practical interpretation.

Many engineers assume that the temperature of hydrocarbon flowing into the wellbore is the same as the reservoir temperature. However, this is not true in reservoirs where high-pressure

drawdown happens. The combination of the various heat transfer mechanisms in the reservoir contributes to the change of the radial temperature distribution because temperature is strongly influenced by fluid properties. There is a potential risk of inaccuracy when estimating the well-productivity, if one does not consider this non-isothermal nature. The analytical solution, including the Joule-Thompson (J-T) effect and heat exchange between the reservoir and its surroundings, will provide the flowing fluid temperature across the reservoir with improved accuracy.

1.3 Research objectives

Heat transfer occurs between fluids, subsurface tubes, and surrounding formations in the wellbore and near-wellbore regions. This research aims to develop tools for field engineers to easily calculate temperatures during drilling circulation, production, and production assisted artificial-lift system. These efficient analytical heat transfer models provide robust solutions with fast computational speeds required for industrial applications. Table 1 illustrates the scope of this research. Modeling the temperature profile in both wellbores and reservoirs is crucial for adequate fluid and equipment design. Other applications include improving the design of production tubulars and artificial-lift systems.

System	Application
Drilling circulation	Near-wellbore cooling effect quantification
Clean-up period	Liquid condensate behavior/Fluid properties identification
Production	Analysis of multiple heat transfer mechanisms in the reservoir
Artificial lift-assisted production	Counter-current heat transfer in the jet pump

Table 1- Scope of this research.

1.4 Outline of the dissertation

This dissertation consists of eight chapters. Chapter 1 introduced the current oil and gas industry trends, problems, and research objectives. Chapter 2 summarizes previous works and limitations. Chapter 3 describes the heat transfer of the tubing-annulus system and presents a representative example of the counter-current flow. An analytical model to estimate the fluid temperature in the tubing and annulus are derived and applied to the jet pump system. Chapter 4 describes the near-wellbore cooling effects by the circulation of cold drilling mud, and the impact of operating parameters on the cooling is analyzed. Chapter 5 shows the fluid behavior interpretation methods with given MDTS data, enabling understating of liquid condensate formation, movement, and collapse. Chapter 6 presents a steady-state heat transfer model in the reservoir system. This chapter contains model validations, sensitivity studies, and analyses of the influence of each heat transfer mechanism. Chapter 7 brings this thesis to an end with a summary and conclusions.

2. LITERATURE REVIEW

2.1 Heat Transfer during Counter-Current Flow: Jet Pump

The nature of shale wells is that production rates rapidly change in a short period, especially in the early stage of production. Because of this dramatic production decline, engineers are struggling to select the optimal artificial lift method, considering the initial production flow rate of the reservoir, gas-oil ratio, and accessibility to the natural gas and compressors. Though gas-lift is also a preferred option in gassier wells like Eagle Ford or Delaware basin, ESPs (Electric Submersible Pumps) have been used primarily in the entire North American field for the artificial lift before converting to rod pump (Kosmicki et al., 2017; Walzel, 2019).

When oil prices are relatively high, ESPs, which can produce a lot in the early stages, even if expensive, are mainly preferred. However, ESPs may not be the appropriate option in the current situation, where oil prices are expected to be in a long-term bear market. In fact, in 2016, many wells in Colombia's Canabe field were inactive in the oil price downturn, despite containing enough reserves for economic purposes. This is because it is more profitable to stop production, given the replacement cost and production loss due to frequent artificial lift failures caused by sand production (Vargas et al., 2018). ESPs are unsuitable for flow with high solid contents because it causes pump failure. These incidents are more frequently reported in the shale field, at least one ESP failure within the first three months of operation in the West Texas shale field (Kosmicki et al., 2017). The cost associated with maintaining ESPs is much higher than the alternatives. Jet pumps may provide operators with a more promising option. During installation, jet pumps need a slickline that eliminates the need to deploy a workover rig, while ESPs require workover. In terms of adaptability, jet pumps are much more cost-effective than ESPs. When the well conditions

change, adjusting throat and nozzle sizes is possible with minimal cost and operational delay. Besides, jet pumps are more reliable than ESPs against not just sandy but also corrosive, gassy, or waxy fluids flow because of the absence of moving parts.

The pioneering theoretical work related to the flow of heat in the wellbore was done by Ramey (1962). He developed an analytical model to calculate fluid temperature as a function of well depth and production or injection rate and time for single-phase liquid or gas flow. His work was later modified by others to avoid long-time approximation of a line source solution (Hasan et al., 1994) and to account for phase change (Satter, 1965) and multi-phase flow (Alves et al., 1992; Hasan et al., 1994). Shiu and Beggs (1980) proposed an empirical correlation to calculate the relaxation distance defined by Ramey. Sagar et al. (1991) extended his model by considering kinetic energy, and Alves et al. (1992) presented a unified temperature prediction model of the flowing fluids in the wells with inclined geometry. These works, however, are only applicable for flow through a single channel.

Jet-pump, like drilling circulation, involves fluid flow in two channels – tubing and annulus. Fluid flow in jet pump systems is similar to that in gas-lift systems where the annulus fluid flows countercurrent to the tubing fluid and adds material (fluid) to the tubing system near the bottom-hole. Countercurrent fluid flow in two adjacent conduits causes complexity in estimating temperatures in the two conduits because of heat exchange between the two conduits' fluids. Holmes and Swift (1970) presented a steady-state model for circulating fluid temperature profiles in the drill pipe and annulus. Kabir et al. (1996) developed an analytical model to estimate temperature profiles in the tubing/annulus system for onshore drilling wells. Hasan and Kabir (1996) also developed an analytical model for flowing temperatures for gas-lift systems. Later, Xu et al. (2020b) applied Hasan and Kabir model to compute the temperature distribution during

drilling circulation in the offshore wells, where two environments with significantly different temperature gradients- cold sea and hot reservoir- make the problem more complicated. Notable among the results these investigators found was that the highest mud temperature in the annulus is at a depth somewhat above the bottom-hole. This is an important finding because the thermal stress that the casing at this depth must bear should be considered for proper design. Yu and Li (2013) proposed a lift system model where light oil instead of gas is used in the annulus to reduce the viscosity of the mixed fluid in ultra-heavy oil reservoirs in China. According to their work, the temperature profile in the annulus does not change much even when the viscosity variations are enormous. They reasoned that the Nusselt number is not dependent on the combined fluid properties in the annulus; thus, the heat transfer coefficient remains unchanged. Many researchers have used the 1996 work of Hasan and Kabir for comparing results or proposing slightly improved analytic models (Hamedi et al., 2011; Mahdiani and Khamehchi, 2016; Mu et al., 2018). Hamedi et al. (2011) proposed a method to enhance the model's accuracy by considering the gas fraction in more detail in obtaining the J-T coefficient. Mahdiani and Khamehchi (2016) showed the improved simulation speed of the Hasan and Kabir model by adding linear regression.

There have been many studies of jet pump systems; however, most of these works concentrate on the principle of working, venturi effect, or determining optimal design parameters using CFD analysis (Fan et al., 2011; Shah et al., 2011; Ji et al., 2015). None of these work attempt to estimate flowing fluid temperature in the two conduits. To the best of our knowledge, no work has presented a method to calculate temperature profiles along with the wellbore for jet pump operating situations.

2.2 Near-Wellbore Cooling Effect by Drilling circulation

Knowledge of the heat transfer between the wellbore and its surrounding is essential not only for drilling and completion but also for many other operations. The following are some of the noteworthy operations where heat transfer plays an important role: optimum design of drilling mud for high-temperature reservoirs, estimation of the hydrocarbon resource volume and optimum production rate, prediction of the gas hydrate zone, well log interpretation, and circulating or producing fluid density (Luheshi, 1983; Shen and Beck, 1986; Hasan and Kabir, 1994; Eppelbaum and Kutasov, 2011; Hasan and Kabir, 2012; Gao et al., 2017; Hasan and Kabir, 2018; Xu et al., 2020a). Drilling operations generally include mud circulation during drilling, followed by completion fluid circulation to remove the mud, which is often followed by a shut-in period. Because drilling mud and completion fluids are pumped from the wellhead, they are usually at around ambient, relatively low temperatures. Thus, upon arrival at the well bottom, they generally cool the near-wellbore region. Even after a few days of shut-in, the near-wellbore region is still usually colder than the undisturbed formation temperature (T_{ei}). Thus, DSTs conducted under these conditions are affected by the near-wellbore temperature that is usually unknown. Any flow test conducted after the drilling circulation period needs to account for the temperature of the entering fluid, which is generally not at the formation temperature.

Focusing on this feature, there have been investigations to predict T_{ei} using the change of wellbore temperature obtained from the temperature logs during shut-in (Dowdle and Cobb, 1975; Kutasov, 1987; Hasan and Kabir, 1994, Santoyo et al., 2000; Yang et al., 2019a). Most of these works relied on temperature data at different shut-in times, used various degrees of complexity and rigor, and predict T_{ei} using the diffusivity equation. A recent model (Yang et al. 2019a) considers the radial temperature gradient of fluids in the wellbore, improving T_{ei} estimation.

In addition to the works for predicting T_{ei}, there have been some studies to estimate temperature distribution near the wellbore. Thus Edwardson et al. (1962) hypothesized, without actual analysis, that temperature disturbances produced by circulation and drilling fluids are limited to within about 10 ft of the wellbore. Lee (1982) and Luheshi (1983) used numerical simulation to distribute a known amount of heat (or cooling) around the wellbore using the diffusivity equation. Recently, Saedi et al. (2019) used the energy balance equation proposed by Kabir et al. (1996) with Neumann and Robin boundary conditions at the bottom-hole to estimate alteration of the geothermal gradient at the wellbore/formation interface. Xu et al. (2020b) proposed a rate estimation method considering the cooled region temperature caused by the drilling circulation. However, they assumed that the radial formation temperature profile is a weighted average of the wellbore temperature and T_{ei}, and that the weighting factor has to be calculated for each field.

As this literature survey shows, the temperature distribution in the circulation-induced cooled near-wellbore area has not received much attention. In addition, the extent of the area affected by cooling from fluid circulation does not seem to have been investigated at all. Estimation of the cooled area is needed to predict the duration of the transient period because the diffusivity equation is valid only for the transient period (Eppelbaum and Kutasov, 2006). Because there have been few quantitative studies, previous research works assumed a constant value for the affected zone and calculated the temperature distribution accordingly (Belrute, 1991; Espinoza et al., 2001; Xu et al., 2020a).

2.3 Sophisticated Completion Tools: MDTS

Distributed Temperature Sensor (DTS) systems, using fiber optics along the wellbore, has been used for over decades, providing essential information for well management and production planning. There have been many applications of DTS data, including steam injection profiling, determination of gas lift valve functionality, tubing leak detection, and behind-the-tubing flow diagnostics (Ouyang and Belanger, 2006; Wang et al., 2008; Wang et al., 2010). However, many authors have pointed out that the resolution of DTS temperature data is often not enough for good quantitative applications, such as flow profiling. There are various reasons for that, including degradation of DTS data, inappropriate integration time, signal degradation from connectors, and hydrogen darkening of the fiber (Wang et al., 2010).

There has been a rapid rise in the use of the data from MDTS in recent years (Kabir et al., 2014; Hashmi et al., 2015; Sayed et al.,2017; Hasan et al., 2018; Christou et al., 2019; Lavery et al., 2019; Xu et al., 2020b). Kabir et al. (2014) showed the usefulness of MDTS-derived rate estimates in performing DST from early-time data with good accuracy. Hashmi et al. (2015) estimated fluid flow rates even from transient MDTS data from four different wells in an Australian offshore field.

Sayed et al. (2017) illustrate the use of continuous transient temperature measurements by MDTS in Egyptian offshore wells. These data were gathered from the pre-perforating stage to the well flow test stage at all pay-zone depths. Subsequently, zonal inflow allocations were conducted using these data. The results of zonal allocation were consistent with the multiple-well tests done during the full flow situation.

An essential aspect of MDTS data from pre- to post-perforation time is understanding these data about near-wellbore cooling due to drilling and circulation. During drilling, fluids at relatively low temperatures are pumped downhole. Since earth temperature increases with depth, the

circulating fluid temperature at the well bottom is often much lower than the surrounding formation. Fluid circulating at lower temperatures than the surrounding significantly cools the bottom-hole, the extent of which depends on circulation rate and time, among other parameters. Hasan et al. (2018) utilized the pre-and post-perforation MDTS data from Sayed et al. (2017) to analyze this near-wellbore cooling and used them for validating the computed temperature profiles in tubing and annulus from their analytic deep-sea drilling model.

2.4 Reservoir Heat Transfer during Fluid flow

Most of the early investigators assumed the fluid temperature in the reservoir was isothermal because the J-T coefficient was much smaller than the fluid specific heat (Xu et al., 2018). However, there were not many reservoirs at high drawdown for comparisons. Early studies attempted to treat heat conduction and convection as the primary heat transfer mechanisms in the reservoir (Lauwerier, 1955; Rubenstein, 1959; Spillette, 1965; Satman et al., 1979).

However, this assumption that fluid temperature remains unchanged during flow may not be applicable for many modern wells, such as deep-water reservoirs with significant. Steffensen and Smith (1973) were the first to discuss the influence of J-T cooling and heating in temperature interpretations. They showed J-T heating occurred in water injection wells, and J-T cooling was observed in gas wells. Data from the 81 DSTs in the North Sea by Hermanrud et al. (1991) supported their findings.

Recently, App (2010) developed a transient numerical model to consider all heat transfer mechanisms in the reservoir, including the J-T effect, adiabatic expansion, and heat exchange with the over- and under-burden formations (Chevarunotai et al., 2018). He emphasized considering fluid property variations due to J-T heating (or cooling) because this can change well productivity.

Ramazanov et al. (2013) proposed a numerical model accounting for the convection, radial heat conduction, and the J-T effect. Their model showed the minimal impact of radial conduction on the fluid temperature with the constant flow rate. App and Yoshioka (2013) proposed an analytical solution in the steady-state for the same problem. They stated the effect of the Peclet number on the fluid temperature profiles in the reservoir. Their results show that the influence of Peclet number on the fluid temperature change is significant where Peclet number is less than one. In contrast, at flow rates where Peclet number is more than three, the impact of Peclet number is minimal.

Analytical models have since been developed, including various heat transfer mechanisms (Onur and Cinar, 2017; Mao and Zeidouni, 2017; Xu et al., 2018; Chevarunotai et al., 2018). Onur and Cinar (2017) presented a transient analytical solution that accounts for the J-T effect and adiabatic expansion but neglects heat exchange with over- and under-burden formations. Mao and Zeidouni (2017) offered similar solutions for near-wellbore damage but excluded the heat exchange between the fluid and the over- and under-burden formations. Xu et al. (2018) revealed the J-T effect is the dominant factor in determining the near-wellbore region, and J-T cooling (or heating) relies on reservoir pressure. It was a little-known fact that J-T heating can happen in the gas reservoir. They showed the J-T effect induces heat even in the gas reservoirs when the pressure is higher than 10,000 psia. Chevarunotai et al. (2018) pointed out that if heat exchange with over- and under-burden formations are neglected, significant error in temperature estimation can occur, especially in long-term production. There are two noteworthy observations in their studies. First, as the flow period increased, the temperature difference keeps increasing when heat loss to the formation is not considered. Second, a further radial distance is required for the fluid temperature to converge to the undisturbed formation temperature. This thermally affected (disturbed) radial

distance is strongly influenced by the flow period, which was also observed in near-wellbore cooling by drilling circulation.

3. HEAT TRANSFER DURING COUNTER-CURRENT FLOW*

3.1 Model Application

Jet pump operation involves injecting a pressurized power fluid (generally a liquid, usually water) through the tubing at the surface. Near the bottom-hole, the pressurized power fluid is passed through a nozzle into the annulus. In some operations, power fluid is injected at the surface through the annulus and passed through a nozzle near the bottom-hole into the tubing. In either case, at the throat of the nozzle, the power fluid's velocity (kinetic energy) increases tremendously, causing a significant pressure drop. This reduced pressure aids reservoir fluid to enter the wellbore to be produced to the surface. The amount of provided pressure difference by jet pumps is shown in Figure 2**.**

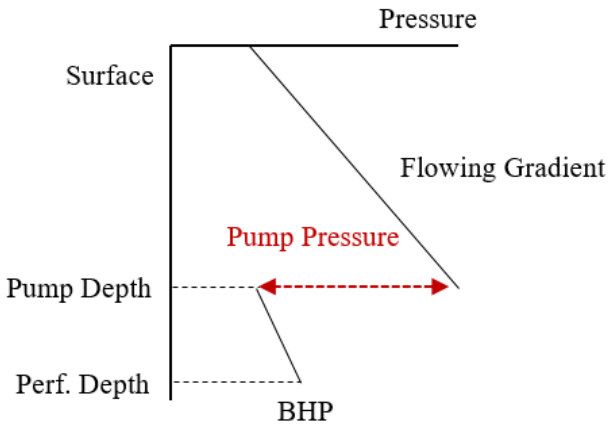

Figure 2- Pressure lift by jet pumps.

* This chapter is from Journal of Petroleum Science and Engineering 203, 108492 "An Analytic Model for Computing the Countercurrent Flow of Heat in Tubing and Annulus System and its Application: Jet Pump" written by Rashid Hasan and Minsoo Jang. It is reprinted here with permission of SPEJ., whose permission is required for further use.

Figure 3 presents the schematic of a control volume indicating fluid flow and heat-transfer with energy balance. In this section, we implement the heat transfer model of Hasan and Kabir (1996) to the jet pump; the assumptions are presented below to set up the mathematical model for jet pumps:

1. Geothermal temperature is a known linear function of depth.
2. Formation has constant thermal properties.
3. Power fluid is liquid with constant thermal properties.
4. Power fluid is injected at the surface through the tubing.
5. Wellbore heat storage effect is neglected.
6. Heat superposition effect is ignored.

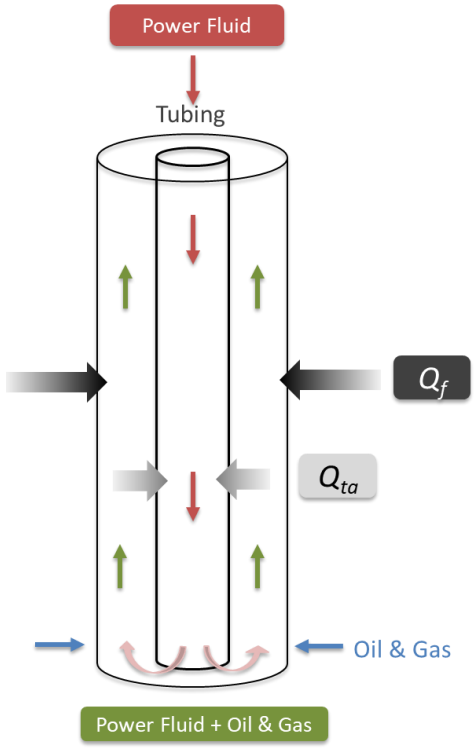

Figure 3- Schematic of heat balance for tubing and annulus.

When power fluid is injected at the surface through the annulus and returns through the tubing, the governing differential equation and the boundary conditions become slightly different. Since the flow direction is the opposite of the proposed in the model from Hasan and Kabir (1996), a little modification on the BC and related constants is made and presented in the Appendix. The final solution in this application for tubing fluid, T_t and annulus fluid T_a temperatures are expressed by Eq. 1 and Eq. 2:

$$T_t = \alpha e^{\lambda_1 z} + \beta e^{\lambda_2 z} + g_G z + B_2 g_G + T_{eiwh} \quad (1)$$

$$T_a = (1 + \lambda_1 B_1)\alpha e^{\lambda_1 z} + (1 + \lambda_2 B_1)\beta e^{\lambda_2 z} + g_G(B_2 + B_1) + g_G z + T_{eiwh} \quad (2)$$

In this application, variables α, β, λ_1, and λ_2 are dependent on BC and surrounding thermal properties. The details of the final solutions and expressions for all the variables are also presented in the Appendix. Figure 4 is a flowchart depicting the calculation processes of temperature and pressure using the aforementioned counter-current flow heat transfer model.

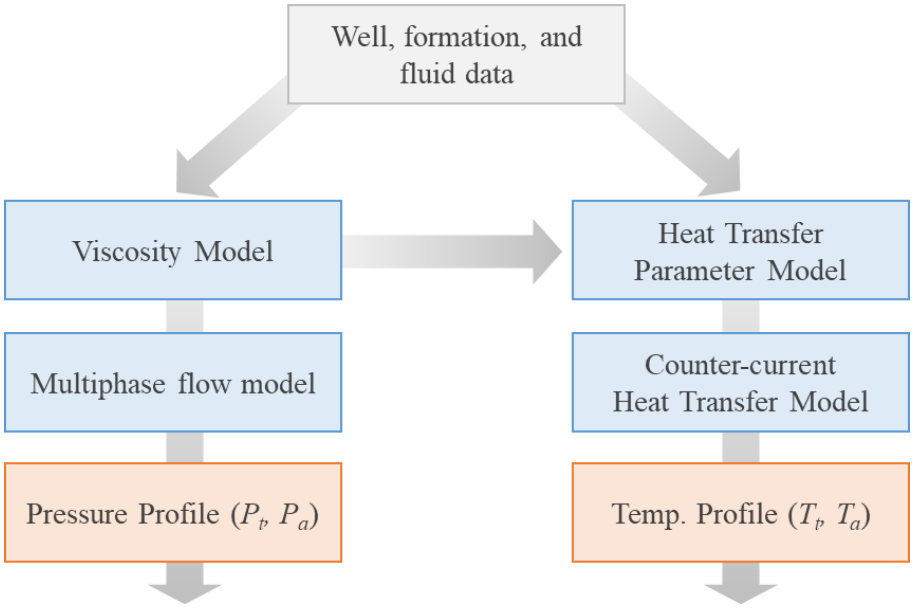

Figure 4- Flowchart for computing temperature and pressure in the tubing and annulus.

3.2 Model Validation

To validate the proposed model, data from a well in the Tah field of the Xinjiang desert in China (Yu and Li, 2013) is used. This well produces 13 °API oil; relevant parameters are shown in Table 2. For effective production, light oil was injected into the annulus, mixed with the reservoir fluid at the bottom-hole, and was produced through the tubing. This well produced a total of 470 STB/d of oil, using 376 STB/d of light oil (80% of total) as the power fluid, injected at a temperature of 176 °F. Figure 5 shows the comparison between the temperature data and results computed by the present model. In Figure 5, the solid gray line represents the geothermal gradient. The black circles are the tubing temperatures measured by sensors located in the tubing. The solid blue line represents the tubing temperature profile estimated using the proposed model. The proposed model shows very good agreement with the field data.

WELL, FORMATION, AND FLUID DATA	
Total well depth, ft	18,040
Casing ID, in.	3.5
Tubing OD, in.	1.5
Oil flow rate, STB/d	470
Light oil density, lb_m/ft^3	51.8
Heavy oil density, lb_m/ft^3	61.2
Tubing thermal conductivity, Btu/hr-°F-ft	25
Casing thermal conductivity, Btu/hr-°F-ft	25
Cement thermal conductivity, Btu/hr-°F-ft	1.01
Earth thermal conductivity, Btu/hr-°F-ft	1.1
Geothermal gradient, °F/ft	0.0104
Bottom-hole temperature, °F	254.2
Surface earth temperature, °F	68

Surface injection temperature, °F	176
Surface injection pressure, psi	432.2

Table 2- Well, formation, and fluid field data for validation.

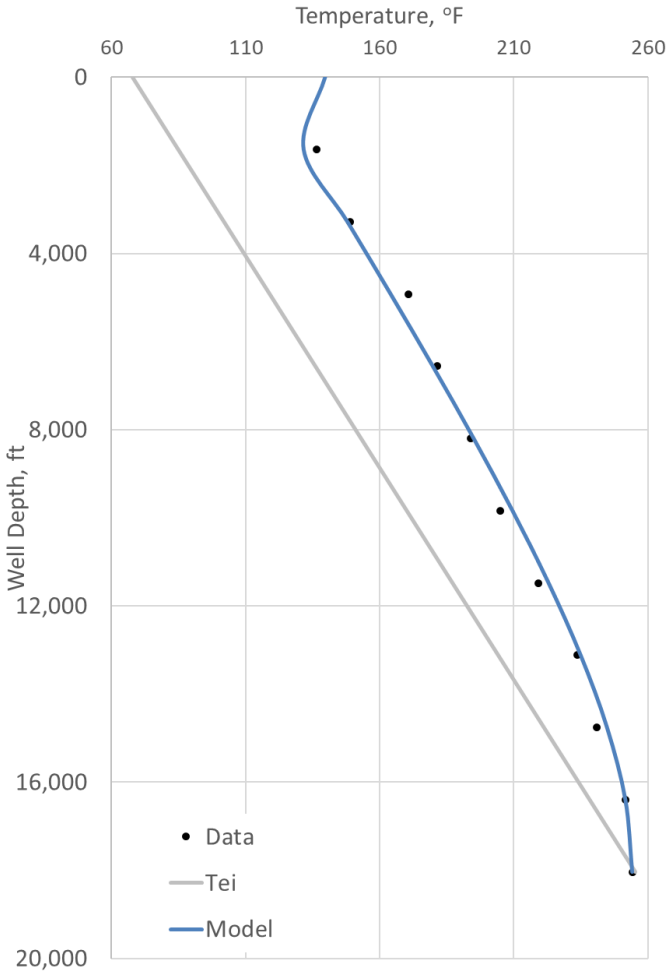

Figure 5- Comparison of predicted temperature profiles by models.

Jet pumps are likely to be installed in legacy wells where the reserves have depleted significantly. Reflecting on this reality, an onshore vertical well in west Texas is used for parametric analysis; pertinent data are presented in Table 3. This is a legacy well reaching the depletion stage, with 109.4 STB/d of oil flow rate, 595 of GLR, and 72% of water-cut. It is producing a relatively light oil of 42 °API gravity. At the wellhead, the power fluid is injected into

the tubing at 2,400 STB/d with a multi-plex pump, at a temperature of 75 °F; reservoir and power fluid are produced through the annulus. There is a temperature sensor installed inside the tubing 18 inches above the bottom-hole. Here, we assume that the measured temperature from the sensor is the same as the tubing temperature at the bottom-hole.

WELL, FORMATION, AND FLUID DATA	
Total well depth, ft	7,400
Casing ID, in.	6.094
Tubing OD, in.	4.5
Oil flow rate, STB/d	10.4
GOR, SCF/BBL	595
Water-cut	0.72
Oil API gravity	42
Gas specific gravity	0.643
Tubing thermal conductivity, Btu/hr-°F-ft	25
Casing thermal conductivity, Btu/hr-°F-ft	25
Cement thermal conductivity, Btu/hr-°F-ft	1.4
Earth thermal conductivity, Btu/hr-°F-ft	0.578
Geothermal gradient, °F/ft	0.011
Bottom-hole temperature, °F	145
Surface earth temperature, °F	70
Surface injection temperature, °F	75
Surface injection pressure, psi	100

Table 3- Well, formation, and fluid field data.

Table 4 presents the various models/correlations used for estimating fluid properties in our proposed model for computing temperature and pressure profiles. The viscosity of hydrocarbon mixture can vary significantly and non-linearly with temperature. Oils containing very heavy

hydrocarbon components, such as bitumen, show a more complex relationship of properties with temperature than those containing lighter components. Therefore, two different viscosity models are implemented for an appropriate comparison. Chew and Conally model is used for lighter oils with API gravity of more than 22, while Hussain model for the heavier oils. Consideration for computing an accurate pressure profile is essential because it determines the amount of free gas in the hydrocarbon mixture at each depth and the limit of injection rate. Hasan and Kabir's multiphase model is utilized for pressure profile computation. Pressure profile computed using Hasan-Kabir model is compared with that computed using Hagedorn and Brown empirical correlation in Figure 6. These two models result in very similar pressure estimation; the maximum difference between the two estimates is about 3%.

Gas compressibility factor	Dranchuk-Purvis-Robinson (1974)
Dead oil viscosity	Chew and Conally (1959)
Live oil viscosity for heavy oil	Hossain et al., (2005)
Friction factor	Chen (1979)
Multi-phase flow	Hasan& Kabir (2012)
Solution gas ratio	Frick (1962)

Table 4- Models used for calculating the temperature profile.

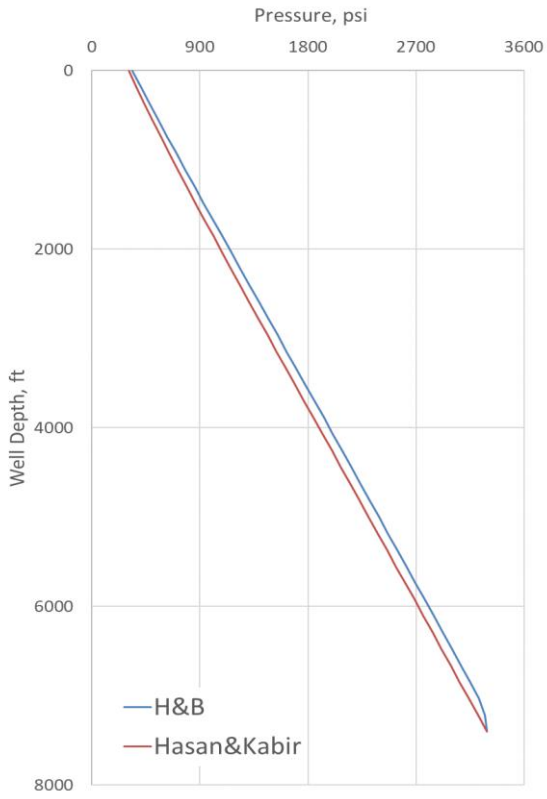

Figure 6- Comparison of pressure profiles from two different models.

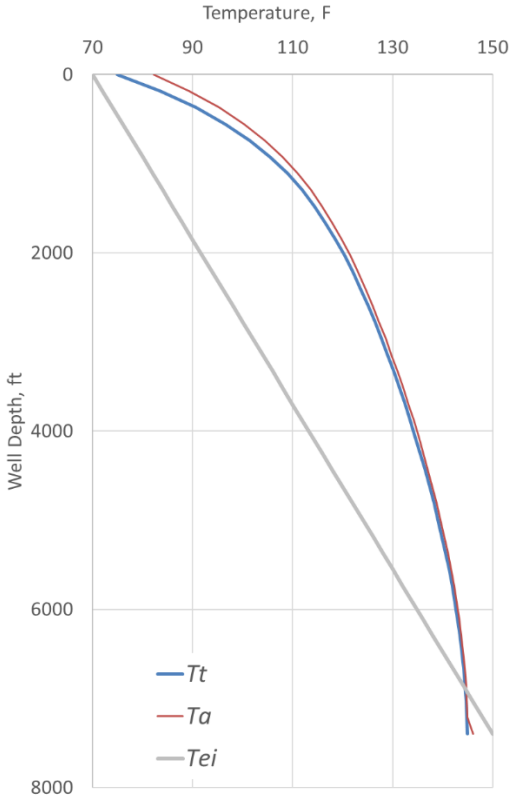

Figure 7- Temperature profiles along the wellbore in tubing and annulus.

Temperature profiles in the tubing and annulus, T_t and T_a, respectively, are shown in Figure 7. Temperatures in both conduits show a concave down shape with depth. Predictably, T_a is larger than T_t at the bottom-hole because hotter reservoir fluid from the formation mixes with the tubing fluid, increasing the mixture temperature that is being produced through the annulus. T_a at the bottom-hole is calculated using a simple heat balance that is presented in the Appendix. The temperature difference between T_t and T_a is very small near the bottom-hole depth region while it is larger closer to the surface. At the wellhead, the difference is around 7~8 degrees. The small difference near the bottom-hole is that the heat capacity of reservoir fluid is not that much different from that of the tubing fluid. The hydrocarbon mixture entering from the reservoir is small, oil

production rate is only about 5% of the injection rate. Installing jet pumps at the very early stage of production in unconventional oil and gas fields has some advantages. That is because production and injection rate ratio can be varied; therefore, the temperature difference between T_t and T_a can be enlarged. The merits of raising producing fluid temperature will be discussed later.

3.3 Application for Heavy Oil

Fluid temperature is an important factor for tubular design and well operations. Its importance is significantly more for heavy oil production because the flow of higher viscosity oils will cause a much higher frictional pressure drop. The strong influence of fluid temperature on its viscosity, and hence friction, increases the importance of temperature estimation for these wells. To show the effect of fluid temperature on oils with various viscosities, we performed some sensitivity analyses.

According to conventional categorization, hydrocarbon mixtures ranging from 8 to 22 ^{o}API are considered heavy oil. The viscosity of oil produced in these wells varies from several hundred to thousands of centipoise; even more, than 10,000 cp, containing bitumen components (Hossain et al., 2005), has been reported. In this section, different viscosity models are implemented depending on the oil's API gravity for computing pressure (and temperature) profiles. Hussain model for oils with 12 to 20 ^{o}API gravity is implemented, while Chew and Conally correlation is used for oils with higher API gravity. Other than these parameters, all input values are the same as in the previous section, presented in Table 3. Figure 8 shows that heavier oil exhibits more significant viscosity variation with temperature. Near the bottom-hole, the three different oils offer relatively little difference in viscosity. However, the gap in viscosity change amongst these oils

widens significantly as depth decreases and is large close to the surface. Note that the extent of non-linearity of viscosity variation with temperature in heavier oils, implying more uncertainty in estimating fluid viscosity for these oils. Thus, accurate temperature estimation along the wellbore is extremely important for heavy oil production systems' operation and design.

Next, we investigate the frictional pressure loss of various oils as they flow up the wellbore, as shown in Figure 9. The trends in frictional pressure gradients of these three oils (API gravities of 12, 20, and 40) are very similar to what was observed about these oils' viscosities in Figure 8. As it is intuitively obvious, heavier oils incur more frictional pressure loss throughout the wellbore. Note, however, that although the viscosity of 12 ^{o}API oil shows more significant change with depth (i.e., temperature) compared to that of 20 ^{o}API oil near the wellhead, the pressure gradients arising from friction for the flow of these two oils do not show that much difference. The reason, of course, is that viscosity changes Reynolds number, which changes the friction factor. However, those changes are less than proportional, resulting in frictional pressure gradients of these two oils showing much less difference.

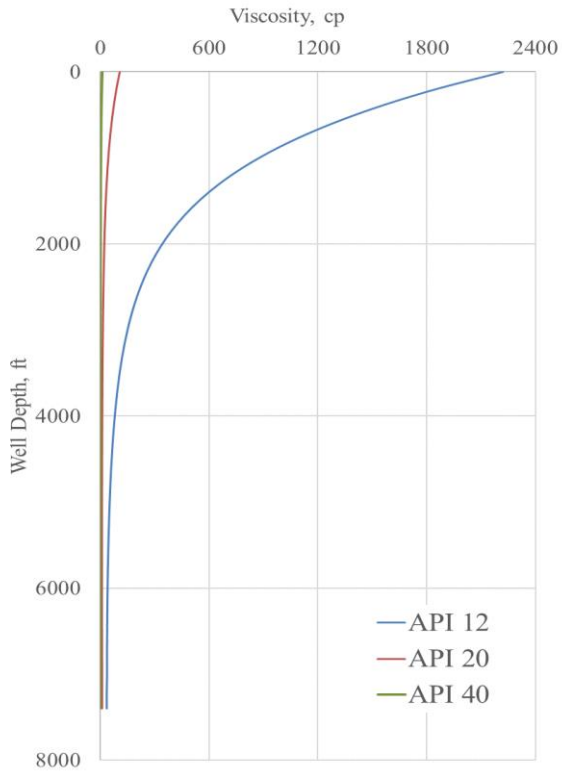

Figure 8- Viscosity variation of oils of various gravity.

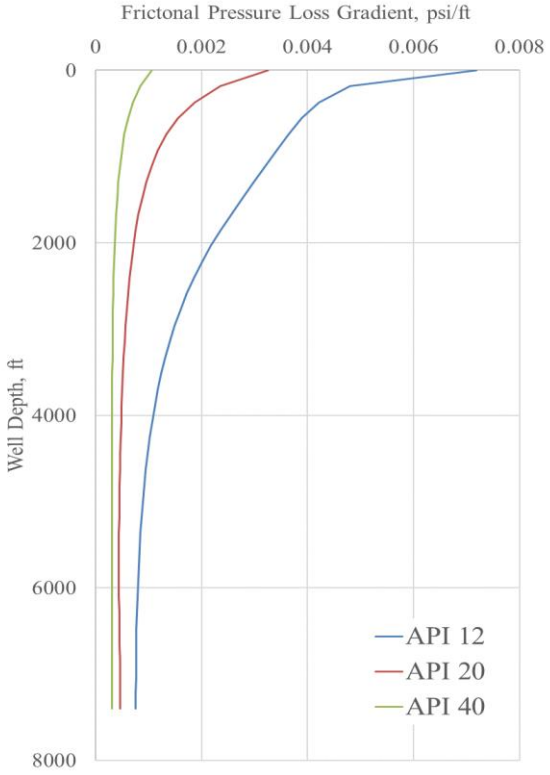

Figure 9- Frictional pressure gradient comparison for the flow of oils of various gravity.

3.4 Sensitivity Analysis

The jet pump operator can control the system's frictional pressure loss to some extent by controlling the fluid injection temperature and rate. In this section, the effect of power fluid inlet temperature and its rate on the annulus fluid temperature profile and frictional pressure loss are analyzed. In Figure 10, the solid lines are the annulus temperature profiles along the wellbore, while solid lines with dots represent the frictional pressure gradient. To show the relationship between the frictional pressure (FP) gradient and the annulus temperature (T_a), the same injecting

temperature (T_{inj}) is displayed in the same color. The reference fluid, 20 ^{o}API oil with a Gas Oil Ratio (GOR) of 595, was lifted by a jet pump using 2,400 STB/d of power fluid, which is water. The temperatures of the injected power fluid are 70, 100, and 125 ^{o}F. Below 3,000 ft, the temperature differences among the three cases are small, meaning that no matter how high the T_{inj}, the annulus fluid temperature (T_a) cannot be larger below this depth. Meanwhile, above the depths of 3,000 ft, the differences in the annulus temperatures among the three different T_{inj} increase as the fluid gets closer to the surface. In the case of 70 and 100 °F of T_{inj}, the shape of the temperature curve is similar to the geothermal gradient, where the temperature decreases as the fluid get closer to the surface.

At the highest tubing fluid injection temperature of 125 °F, the shape of the fluid temperature profile is different from the other two cases. Figure 10 shows that when the T_{inj} is 125 °F, the T_a increases with decreasing depth for depths below 1,000 ft. This is opposite to the trends evident for lower fluid injection temperatures. The reason for this annulus fluid temperature profile curvature change, of course, is that T_a depends on its heat transfer with the surrounding formation and the tubing fluid. Because of much lower overall heat transfer resistance between the tubing and annulus fluids compared to that between the annulus fluid and the formation, T_a is significantly more influenced by the tubing fluid temperature than the formation temperature at these depths.

For the case when the T_{inj} is 125 °F, the annulus fluid gains more heat from the tubing fluid than it loses to the surrounding – and this gain rapidly increases as the annulus fluid approaches the wellhead. However, further down the well, the formation temperature becomes higher than the T_a, and the pattern becomes similar to the other two cases. This is further explained later with reference to Figure 11. The high value of the T_a near the surface (125 ^{o}F at the surface) causes the

produced fluid temperature to gradually increase as it gets close to the surface. This increased value of temperature near the surface causes a lowering of viscosity, which, in turn, causes a decreased frictional gradient. Therefore, when the T_{inj} is 125 ^{o}F, the frictional pressure gradient at the surface is around 30% lower than when the T_{inj} is 75 ^{o}F.

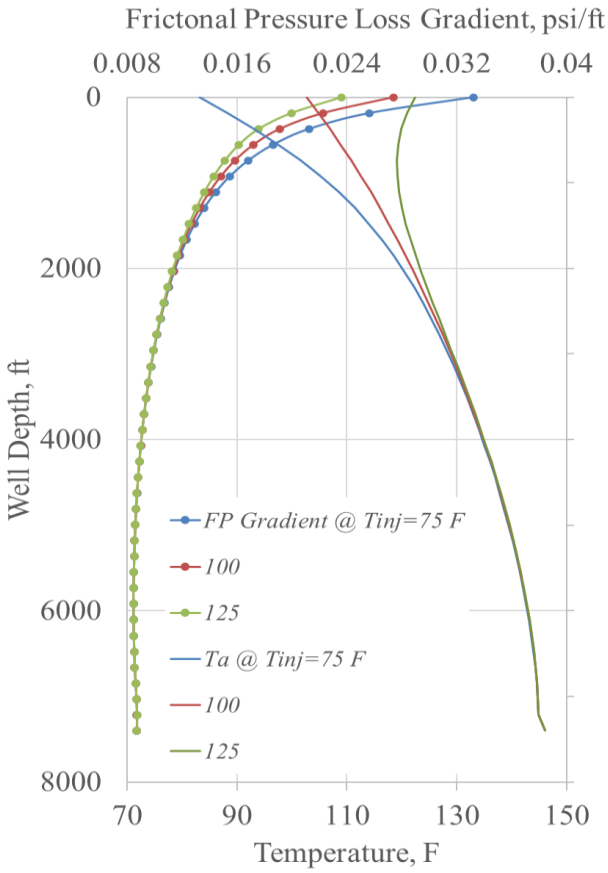

Figure 10- Influence of tubing injection temperature upon frictional pressure drop in the annulus.

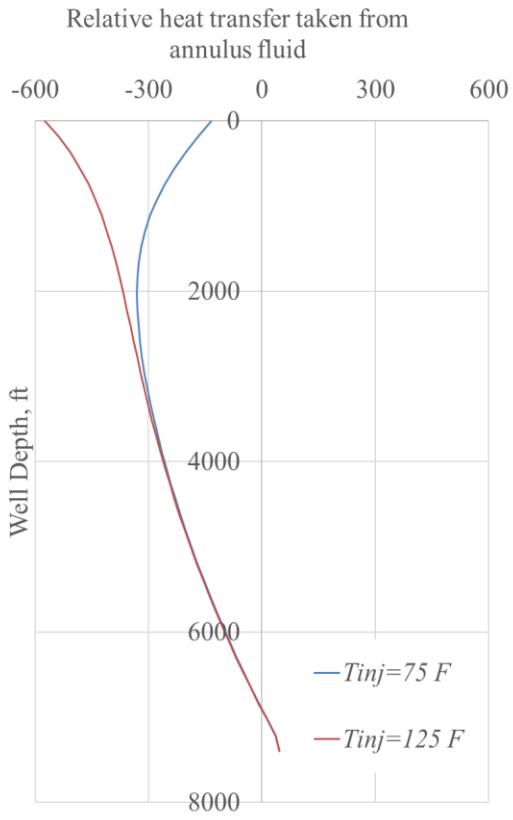

Figure 11- Heat transfer from the annulus to the formation.

Figure 11 shows the relative amount of heat transfer from the annulus to the surrounding formation for two different injection fluid temperatures. As expected, when the injecting fluid temperature is 125 °F, heat loss from the fluid to the surrounding, near the surface is much higher than when the injecting fluid temperature is 75 ^{o}F. For the higher inlet temperature, fluid heat loss continually decreases with depth as the fluid encounters higher temperature surrounding – and finally becomes negative (i.e., fluid gains heat from the surrounding) near the bottom-hole. For the lower (75 ^{o}F) inlet temperature case, the situation is slightly more complex as the lower temperature tubing fluid near the surface gains more heat from the annulus fluid, causing annulus fluid heat loss to increase initially with depth. However, after a certain depth, the shape of the curve becomes similar to that of the other case.

Injection rate is another factor that can be adjusted to influence fluid temperature, and hence, its viscosity and friction pressure loss. Figure 12shows fluid temperature and frictional pressure gradient along the well for three different power fluid flow rates: 1,600, 2,400, and 3,200 STB/d. Higher flow rates increase velocity, which exponentially increases frictional pressure gradient. Higher velocity also means fluid spends lesser time in the system. In addition, because injecting fluid temperature is generally lower than the reservoir temperature, mixed fluid temperature is lower for higher injection (power fluid) rate because of shorter heat exchange time. This lowering of temperature also increases friction pressure loss because of increased viscosity. Figure 11 shows that the cooling effect near the bottom-hole is small, causing a small frictional pressure gradient change. However, near the surface, the effect of higher flow rates increasing frictional gradient is clear in Figure 11. To summarize these results, the injection flow rate has a greater influence on the frictional pressure loss than the T_{inj}. In addition, computing the pressure

loss is essential when considering changing the flow rate since the pressure loss goes up exponentially with the rate.

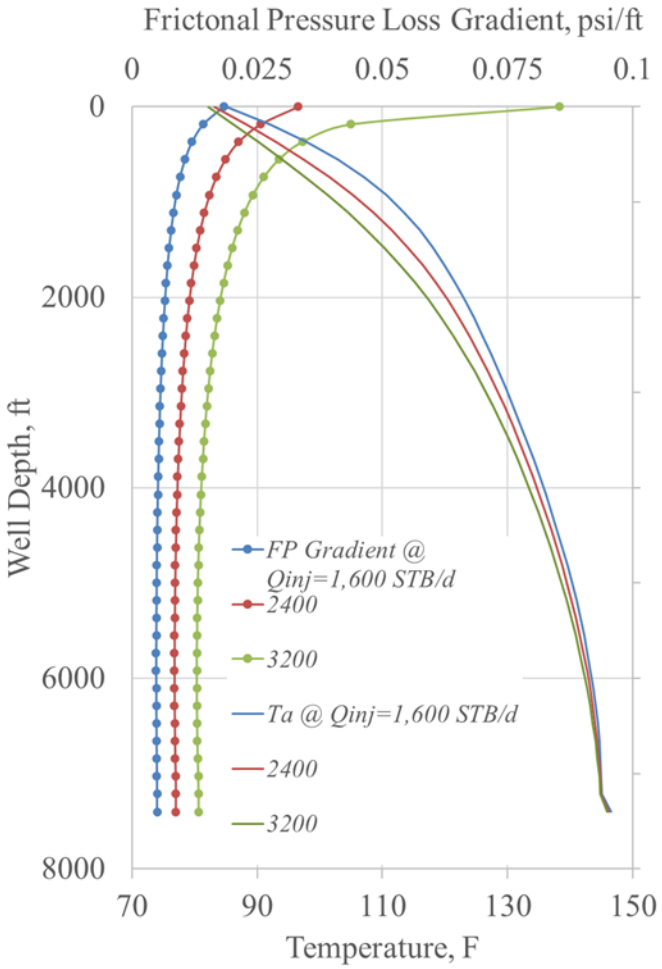

Figure 12- Influence of tubing injection rate upon frictional pressure drop in the annulus.

3.5 Comparison of Results for Various BC

The analytical solution based on the energy balance presented here provides accurate temperature estimates with minimal computation cost. The proposed model requires two boundary conditions (BC) to solve because it is based on a second-order differential equation, as explained in the Appendix. Wellhead and bottom-hole fluid temperatures (either of the tubing or the annulus)

are the best boundary conditions from the perspective of the robustness of the solution; we consider this to be Case 1. Typically, jet pumps are implemented in the wells where production has decreased significantly; therefore, the operators are not likely to invest too much money for measuring temperatures, particularly at the bottom-hole. For fluid circulation, the derivative of the fluid temperature at the bottom-hole is taken as zero ($dT_t/dz = 0$) because the same fluid exiting the tubing enters the annulus at that location (Kabir et al., 1996; Xu et al., 2020b). In the Jet pump case, because fluid from the reservoir – with differing thermal properties – mix with the power fluid to form the fluid mixture that would be produced, dT_t/dz is not zero here. However, if the fluid properties are not too different or the amount of reservoir fluid is much smaller than that of the power fluid $dT_t/dz = 0$ at the bottom-hole is a good approximation. That forms our Case 2. Gathering temperature data at the wellhead imposes a minimal cost. Thus, the third case of BC would be using temperature data of the fluids at the wellhead of the tubing and annulus; that is considered Case 3. The three cases are shown in Table 5.

Case	BC 1	BC 2
1	Tubing temp. at the surface (T_{twh})	Tubing temp. at the bottom-hole (T_{tbh})
2	Tubing temp. at the surface (T_{twh})	Tubing temp. gradient at the bottom-hole (dT_t/dz)
3	Tubing temp. at the surface (T_{twh})	Annulus temp. at the surface (T_{awh})

Table 5- BC cases for temperature profiles comparison.

In the following section, we investigate the differences in model estimated temperature profiles when this three different BC are applied; Figure 13 shows the annulus temperature distribution for these three cases. For the entire well, the difference between Case 1 and 2 is not

significant. However, Case 3 shows higher temperatures throughout the wellbore than in the other two cases. For more precise comparisons of the tubing and annulus temperature profiles, the plot of temperature versus depth from 6,000 ft to 7,500 ft are shown in Figure 14 (tubing) and Figure 15 (annulus). Temperature profiles in Figure 14 and Figure 15 are very similar; however, annulus temperature is higher, especially near the bottom-hole, because higher temperature reservoir fluid mixes with the annulus fluid.

It is interesting to examine Case 3 in Figure 13, which shows significantly higher temperature estimates compared to the other two cases often more than 10 ^{o}F. This is observed especially near the bottom-hole. This overestimation for Case 3 BC is an indication of a lack of robustness for this set of BC. Another noteworthy phenomenon for Case 3 is the slope change in the temperature profile around well depths of 7,100 ft. to 7,300 ft. All these computations have used the usual geothermal gradient that allows formation temperature to increase with depth. Also, as long as the formation temperature keeps increasing with depth, both the tubing and annulus fluid temperatures keep increasing. The opposite trend at the aforementioned depth for the fluid temperatures estimated using Case 3 BC clearly indicates that it is an unreliable set of boundary conditions.

The unreliability of the Case 3 boundary condition is that the fluid temperatures in the annulus and the tubing are very similar because of the low thermal resistance between them. In other words, the two BC are not entirely independent. Mathematically, that means when the wellhead tubing and annulus fluid temperatures are used as boundary conditions, the set of differential equations become ill-posed.

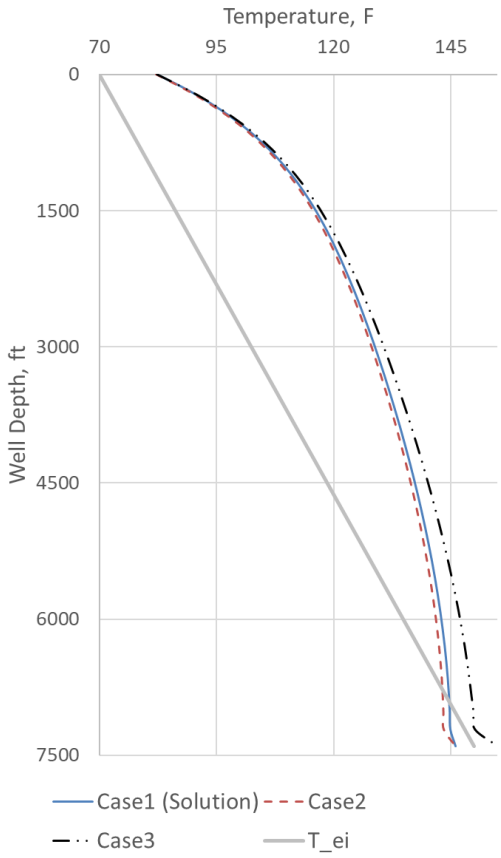

Figure 13- Annulus temp. profile along the whole depth with the three BC cases.

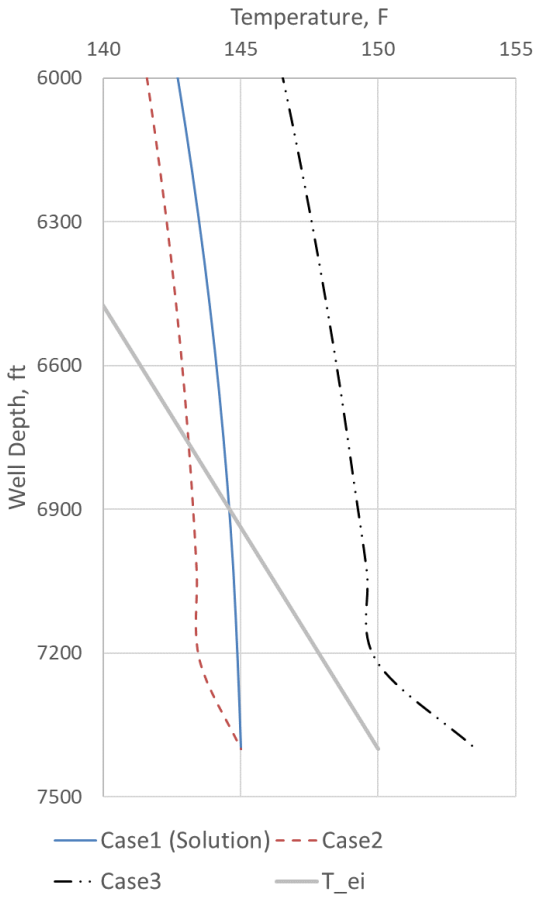

Figure 14- Tubing temp. profile at near-bottom-hole depth section with the three BC cases.

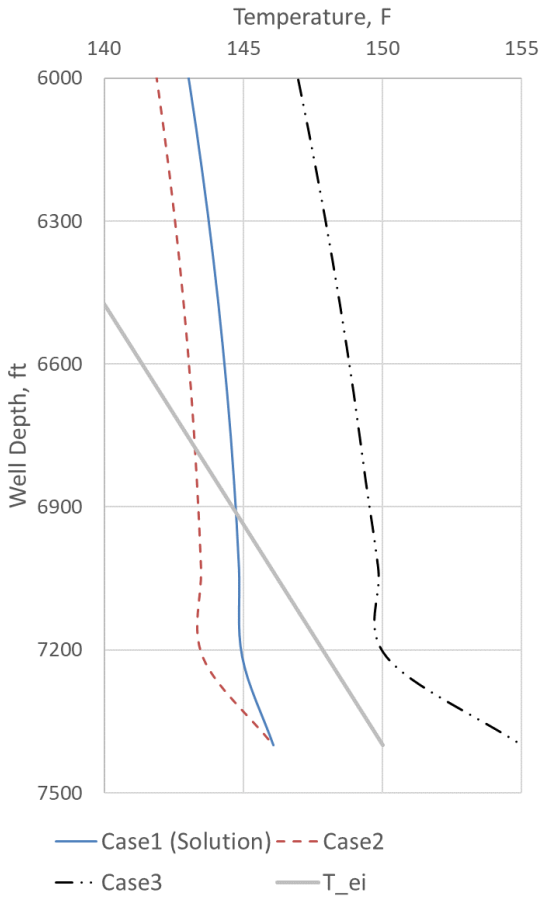

Figure 15- Annulus temp. profile in near-bottom-hole depth section with the three BC cases.

3.6 Numerical Iteration for Insufficient BC

The previous section discussed the need for temperature data in the bottom-hole area to use the proposed model. In this section, we offer a method for predicting the temperature distribution throughout the well in the absence of subsurface temperature measuring devices. As is often the case, the proposed method assumes that the temperature of the reservoir fluid entering the wellbore is available. In this method, first, we assume a reasonable temperature value at the tubing bottom-

hole (T_{tbh}). Given that, the annulus bottom-hole temperature (T_{abh}) can be obtained from the heat balance of the mixture of entering reservoir fluid and power fluid, as shown in the Appendix. This allows the model to calculate the wellhead annulus fluid temperature, T_{awh}. If the difference between the calculated wellhead temperature and the actual one is not small enough, the T_{tbh} is changed, and the T_{awh} is recalculated. Iteration is continued until the difference between the previously calculated wellhead temperature and the actual one becomes smaller than an error tolerance, as shown in Figure 16.

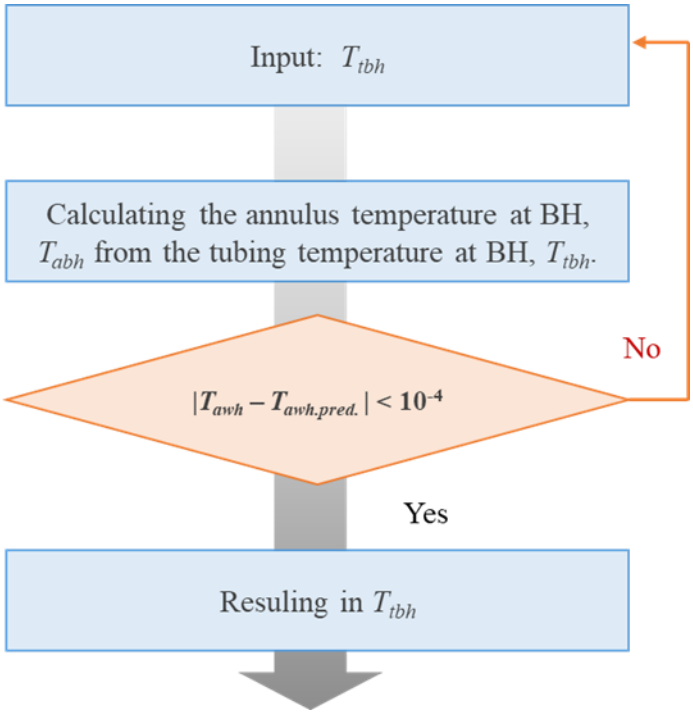

Figure 16- Flowchart for calculating the bottom-hole temperature.

Table 6 shows the bottom-hole and wellhead temperatures obtained through the proposed numerical iteration with 10^{-4} of error tolerance. The five cases of assumed T_{tbh} are used for the

analysis, which is in the first column, and the T_{awh} values for them in the following column of Table 5. The proposed iteration method predicted T_{tbh} values with a consistent error of only 0.04%. Given the little error, the proposed iteration method can predict bottom-hole temperature accurately without any subsurface measurement. Note that this approach is still using two data as BC – the wellhead fluid temperature and the entering reservoir fluid temperature.

Bottom-hole Temp. (T_{tbh})	Wellhead Temp. (T_{awh})	Predicted Bottom-hole Temp. ($T_{tbh\_predicted}$)	Error (%)
135	81.72	134.95	0.037%
137.5	81.85	137.44	0.042%
140	81.98	139.94	0.044%
142.5	82.11	142.44	0.044%
145	82.24	144.94	0.043%

Table 6- Results of related values after iterations.

4. NEAR-WELLBORE COOLING EFFECT

4.1 Model Development

We treat the formation as a homogeneous solid to model heat flow and the resulting temperature distribution in such systems. Assuming symmetry around the well simplifies the three-dimensional (3D) problem to a two-dimensional (2D) one. Besides, heat diffusion in the vertical direction may be ignored, owing to small vertical temperature gradients. Neglecting vertical heat flow reduces the system to a one-dimensional (1D) heat-diffusion problem. This approach, adopted by Hasan and Kabir (1994) and others, introduces very little error and allows an analytical solution for the problem. Figure 17 represents the system being modeled, showing a thermally affected zone of radius, r_a, where all of the formation temperature change occurs.

An energy balance on the formation then leads to the partial-differential equation, derived

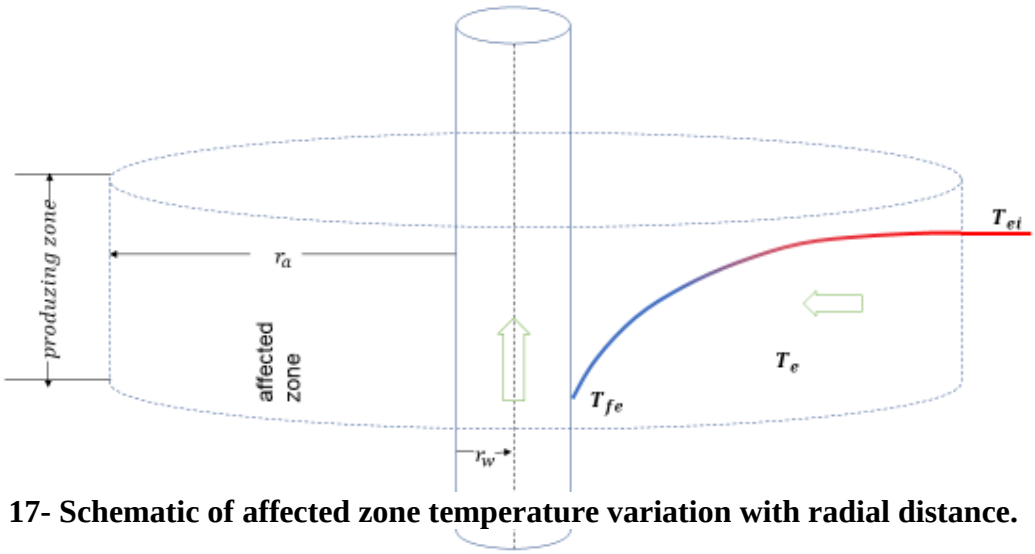

Figure 17- Schematic of affected zone temperature variation with radial distance.

in cylindrical coordinates, for the variation of formation temperature with radial distance from the well and time,

$$\frac{c_e \rho_e}{K_e}\frac{\partial T_e}{\partial t} = \frac{1}{r}\frac{\partial T_e}{\partial r} + \frac{\partial^2 T_e}{\partial r^2}. \tag{3}$$

For a line-source, the solution for constant heat flow rate Q, is,

$$T(t,r) = T_{ei} - \frac{Q}{4\pi K_e} E_i\left(-\frac{c_e \rho_e r^2}{K_e t}\right). \tag{4}$$

Using log approximation of the *Ei* function gives,

$$T(t,r) = T_{ei} - \frac{Q}{4\pi K_e} ln\left(\gamma \frac{c_e \rho_e r^2}{K_e t}\right). \tag{5}$$

We make the further assumption that all the near-wellbore cooling happens in an affected zone in which radial distance from the wellbore center is r_a, the affected region radius. At the wellbore boundary, when $r = r_w$, we have $T = T_w$. Therefore, total temperature drop – the difference between wellbore temperature and the undisturbed formation one, ΔT (= $T_{rw} - T_{ei}$) – equals

$$\Delta T = T(t,r_a) - T(t,r_w) = \frac{Q}{4\pi K_e} ln\left(\frac{r_a^2}{r_w^2}\right). \tag{6}$$

Our assumption is that at $r = r_a$, T becomes T_{ei}. Hence,

$$\begin{gathered} T(t,r_a) - T(t,r) = \frac{Q}{4\pi K_e} ln\left(\frac{r_a^2}{r^2}\right), \\ T(t,r) = T(t,r_a) - \frac{Q}{4\pi K_e} ln\left(\frac{r_a^2}{r^2}\right) = T_{ei} - \frac{Q}{4\pi K_e} ln\left(\frac{r_a^2}{r^2}\right). \end{gathered} \tag{7}$$

Hence, temperature at any radial position T_r, divided by total temperature drop, ΔT, is

$$\frac{T_r}{\Delta T} = \frac{T_{ei}}{\Delta T} - ln\left(\frac{r_a^2}{r^2}\right) \Big/ ln\left(\frac{r_a^2}{r_w^2}\right), \tag{8}$$

$$T_r = T_{ei} - \Delta T \left. ln\left(\frac{r_a^2}{r^2}\right) \middle/ ln\left(\frac{r_a^2}{r_w^2}\right). \right.$$

Eq. 8 allows the computation of the temperature profile if ΔT (= $T_{rw} - T_{ei}$) data as a function of time is available, as is the case in many intelligent wells.

Energy Balance

The amount of cooling per foot of well, *dQ*, that has happened in the section bounded by radii *r* and *r*+*dr* is given by,

$$dQ = mc_e(T - T_{ei}) = \pi((r + dr)^2 - r^2)\rho_e c_e(T - T_{ei}). \quad (9)$$

Total cooling can then be obtained through numerical integration over the radii r_w and r_a:

$$Q = 2\pi\rho_e c_e \int_{r_w}^{r_a} (T - T_{ei}) r dr, \quad (10)$$

or,

$$Q = \pi\rho_e c_e \sum_{r_w}^{r_a} (r_{i+1}^2 - r_i^2)\,(T - T_{ei})_{avg}. \quad (11)$$

The total near-wellbore cooling, *Q*, given by Eq. 11, has to result from the heat lost by the formation to the wellbore during circulation. The analytical model proposed by Xu et al. (2020b) allows this *Q* estimation at any given position in the well for the general case of a deep-water well. That estimated value of *Q*, along with Eq. 11 allows computation of r_a. A sample calculation of the proposed method is presented in the Appendix.

4.2 Model Validation

Actual data for radial temperature in the formation after circulation is practically impossible to obtain because of cost. Therefore, the proposed model is validated using simulation results of the numerical model of Yang et al. (2019b). Table 7 reports the parameters used to generate the synthetic field data using the Yang et al. (2019b) model. This well is in a relatively deep and high-temperature reservoir with a bottom-hole temperature of approximately 275 ^{o}F at a depth of 16,000 ft, and 240 GPM of mud is injected and circulated for 10 hours.

Figure 18 compares the estimates of our model (blue line) with data generated using Yang et al. (2019b)'s numerical model (red circles). Excellent agreement of the model with the synthetic data is evident from Figure 18. Besides, the model predicts a value of 7.47 ft for the affected radius, r_a, which is within the hypothesized range recommended by Yang et al. (2019b). They commented that while the value of r_a is not precisely known, it is between 7 and 19 ft. This estimation is based on their simulation that showed formation temperature changes very little in that range. Another notable observation is that the temperature change is larger near the wellbore, gradually becoming smaller away from the wellbore, asymptotically approaching, T_{ei}, the static reservoir temperature.

	Value
Well depth, ft	16,076
Drill-pipe ID, in.	4.78
Drill-pipe OD, in.	5.50
Open-hole radius, in.	8.27
Mud thermal conductivity, Btu/(h-ft-°F)	0.722
Mud specific heat, Btu/(lb-°F)	0.382
Mud density, lb_m/ft^3	74.9
Cement thermal conductivity, Btu/(h-ft-°F)	0.404
Cement specific heat, Btu/(lb-°F)	0.478
Formation thermal conductivity, Btu/(h-ft-°F)	1.300

Formation specific heat, Btu/(lb-°F)	0.191
Formation density, lb_m/ft^3	164.8
Geothermal gradient, °F/ft	0.012
Surface temperature, °F	77
Injection temperature, °F	86
Circulation rate, GPM	237.6
Circulation time, hr	10

Table 7- Well, formation, and fluid data for validation.

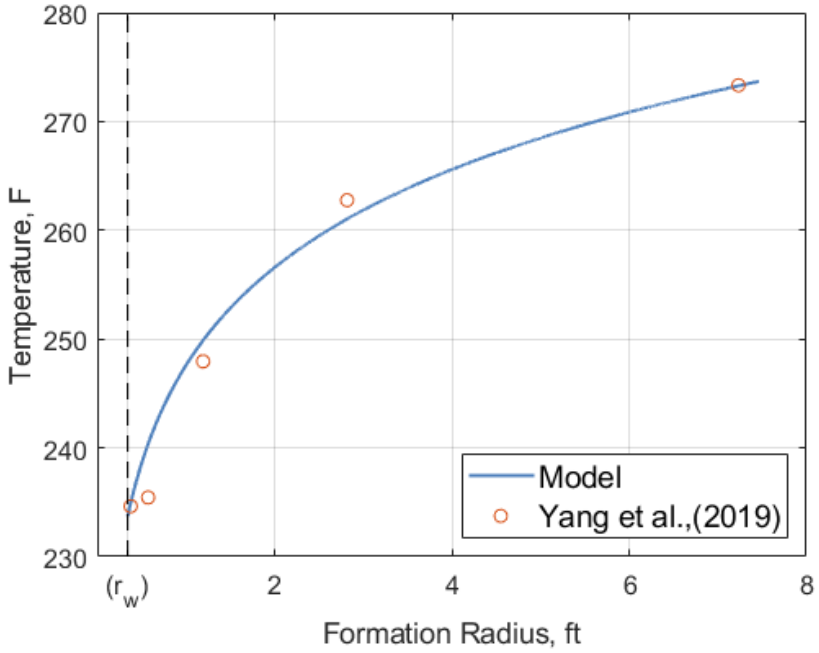

Figure 18- The comparison of temperature distribution between the proposed model and data.

4.3 Sample Calculation.

In this section, stepwise calculations of the affected radius, r_a, is described. For sample calculations, we are using the data from the field case presented by Xu et al. (2020b) that offers realistic bottom-hole temperature data as well as circulation rate and time. The related well geometry, formation thermal properties, and circulation information are summarized in Table 8. The well is vertical, with a true vertical depth of 13,652 ft, including a seawater depth of 5,118 ft

where the wellhead facilities are equipped. 500 GPM (gallons per minute) of mud is circulated for one week (168 hours). This calculation is conducted at the bottom-hole depth, where the undisturbed formation temperature, T_{ei}, is 144.84 ^{o}F, and temperatures in the annulus and tubing (= inner drilling pipe) are 81.72 ^{o}F.

The total amount of heat transferred during the 168 hours of circulation can be obtained by multiplying the duration of circulation by the formation heat loss per hour. Using the analytical model proposed by Xu et al. (2020b), we calculated this formation heat loss to be 113.5 Btu ft^{-1} h^{-1}. Thus, the total amount of heat transferred during 168 hours equals,

$$Q_{circ} = (113.5)(168) = 19{,}068\ \frac{Btu}{ft}.$$

For computing the total cooling effect on the reservoir following Eq. 9, we need to calculate the temperature profile along the reservoir's radial direction. In Eq. 6, the variable radius, r, is between the wellbore radius and the affected radius, r_w and r_a,. The radius is discretized into a number of segments with sub-index i.

Parameter	Value
True vertical depth, ft	13,652
Sea depth, ft	5,118
Casing shoe depth, ft	12,867
Perforation zone, ft	13,100 - 13,396
Wellbore radius, in.	5.875
Formation thermal conductivity, Btu/(h-ft-°F)	0.578

Formation specific heat, Btu/(lb_m-°F)	0.215
Formation specific density, lb_m/ft^3	2.65
Circulation flow rate, GPM	500
Circulation time, hr	168
Undisturbed formation temperature (T_{ei}), °F	144.84
Annulus temperature, °F	81.72
Heat flow at the bottom-hole, Btu/(h-ft)	113.5

Table 8- Well geometry, formation thermal properties, and circulation information.

$$T_i = T_{ei} - \Delta T \frac{ln\left(\frac{r_a^2}{r_i^2}\right)}{ln\left(\frac{r_a^2}{r_w^2}\right)},$$

where

$$\Delta T = T_{ei} - T_{ann} = 144.84 - 81.72 = 63.12$$

$$r_1 = r_w + 0.001\,, r_2 = r_w + 0.002, .., \qquad r_n = r_a$$

The cooling effect on the reservoir, Q_e, can be calculated by combining all the discretized Q obtained using Eq. 11. Using formation material density, ρ_e of 143.52 lb_m/ft^3 and specific heat, c_e = 0.215 Btu/(lb-°F).

Computation is performed by increasing r_a until the Q_e matches with Q_{circ} within a tolerance of less than 1% of the difference between Q_e and Q_{circ}. This procedure resulted in the temperature distribution in the radial direction from the wellbore to the formation, as shown in Figure 19. As expected, the temperature change is larger near the wellbore, gradually becomes smaller away from the wellbore, and asymptotically converges to the reservoir's static temperature. A computed value of 7.993 ft for the affected radius at the bottom-hole was obtained.

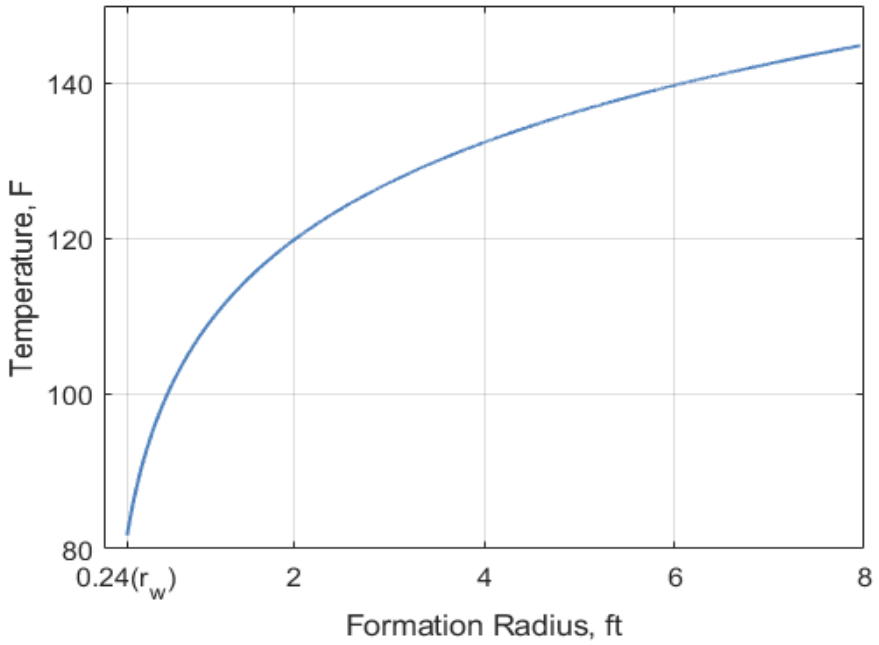

Figure 19- Temperature distribution along the formation due to circulation induced cooling.

4.4 Sensitivity Analysis

Critical operating parameters for drilling circulation are flow rate, circulation time, and injecting mud temperature. Amongst these three operating variables, the injecting mud temperature

from the surface had little influence on the temperature change of the fluid in the wellbore, as was pointed out by previous studies (Xu et al., 2020b; Jang and Hasan, 2020). This minimal effect of injecting fluid temperature is primarily due to the characteristics of offshore wells. Even if high-temperature mud is injected, most of the heat is lost in the riser near the fluid contact with the cold seawater having a large heat capacity. When the mud goes near the sea bottom, its temperature becomes virtually the same as that of the seawater.

Figure 20 describes the change in the value of the thermally affected radius, r_a, with circulation time when the flow rate is 100 GPM. As one would think intuitively, Figure 20 shows that, as circulation time increases, cooling increases, and so does the affected radius r_a. For example, as circulation time increased from one day to seven days, r_a increases to almost three

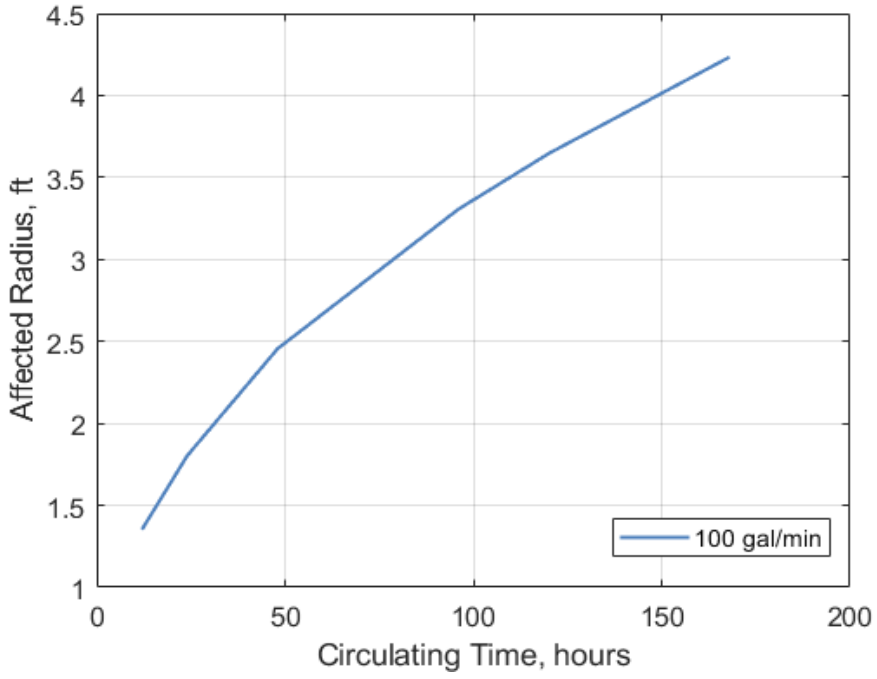

Figure 20- Thermally affected radius change with circulating time.

times the one-day value. Also, the rate of increase in r_a decreases very slightly as the circulation time is increased.

Figure 21 presents the change in the value of r_a with flow rates when the circulation time is one week (168 hours). In this case, one would think that as the circulation rate increases, cooling will increase, and so should the affected radius r_a. However, Figure 21 shows that when the flow rate increases from 100 to 500 GPM, r_a increases from 7.978 ft to about 7.987 ft; an increase of only 0.12% for a fivefold increase in rate. Further rate increase induces even lesser changes in r_a, until r_a becomes almost constant.

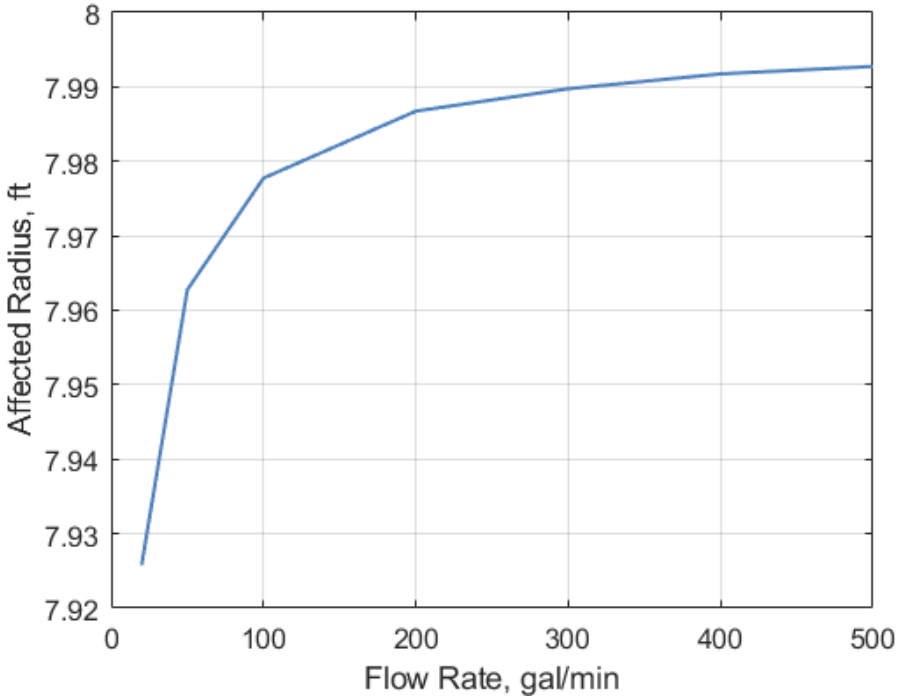

Figure 21- Thermally affected radius change with flow rates.

These results, presented in the two figures, appear to contradict each other. Both circulation time and rate affect near-wellbore cooling similarly, yet circulation time has so much more effect on affected zone radius than does rate. Three cases of different flow rates and circulation times are investigated to analyze the seemingly conflicting effects of these two operating variables. The results of these investigations are presented in Table 9. Our analyses show that, although a higher

circulation rate cools the formation around the wellbore more – i.e., near-wellbore ΔT becomes larger – a higher rate also increases the amount of heat transfer during circulation (Q_{circ}). The absence of a difference in r_a can be explained from the examination of Eq. 11; a higher flow rate results in a more enormous temperature difference between the wellbore and the formation (ΔT). This will inevitably lead to a smaller size of the term for the circular area, $r^2_{i+1} - r^2_i$, which increases rapidly as the sub-index i get larger. In short, the Q_{circ} is larger, but the difference in r_a is little because the ΔT is also larger. A similar increase in both ΔT and Q_{circ}, – which are on the opposite sides of the equation – leads to a very small change in the term for the circular area, $r^2_{i+1} - r^2_i$,. In short, the Q_{circ} is larger, but the difference in r_a is little because ΔT is also larger.

Case No.	Flow Rate, GPM	Circ. Time, hour	r_a, ft	Q_{circ}, Btu/ft	ΔT, °F
1	100	168	7.978	9,928	32.9
2	500	168	7.993	19,370	64.1
3	100	84	4.715	5,536	30.8

Table 9- Related variables for sensitivity analysis.

Another way of looking at this phenomenon is to note the fundamental difference in the effect of the two variables – circulation rate and time – is that while both increase near-wellbore heat transfer, longer circulation time allows heat to flow outward from the wellbore – thus increasing r_a. However, the increased flow rate does not allow the time for heat exchange to propagate too far into the formation.

5. MDTS APPLICATIONS

Analysis of DTS data has been hampered because differing thermal properties of various components of the produced fluid in the perforated intervals have been ignored, leading to significant zonal rate estimation errors. However, one of the fundamental problems of deploying fiber optics DTS lies in its fragile nature that makes them inapplicable. MDTS has emerged to overcome this limitation through its sturdy nature. Besides, a temperature resolution of 0.004 °C with no drift provides much more accurate and reliable data. Additionally, this advanced temperature measuring system can provide data with excellent spatial resolution within multiple perforated zones.

5.1 Schematic of MDTS

Figure 22 below illustrates the schematic of MDTS equipment which runs through the hole and measures the temperature. In this case, 160 temperature sensors (highlighted by the red dashed line), phased 180^{o}, are clamped to the Tubing Conveyed Perforating (TCP) gun. The effective spacing of these sensors is about one foot, allowing coverage of the whole perforating depth. High-resolution pressure gauges above and below the perforated interval and above and below the tester valve were also used. Using an acoustic communication system, real-time temperature and pressure data were available during the DSTs.

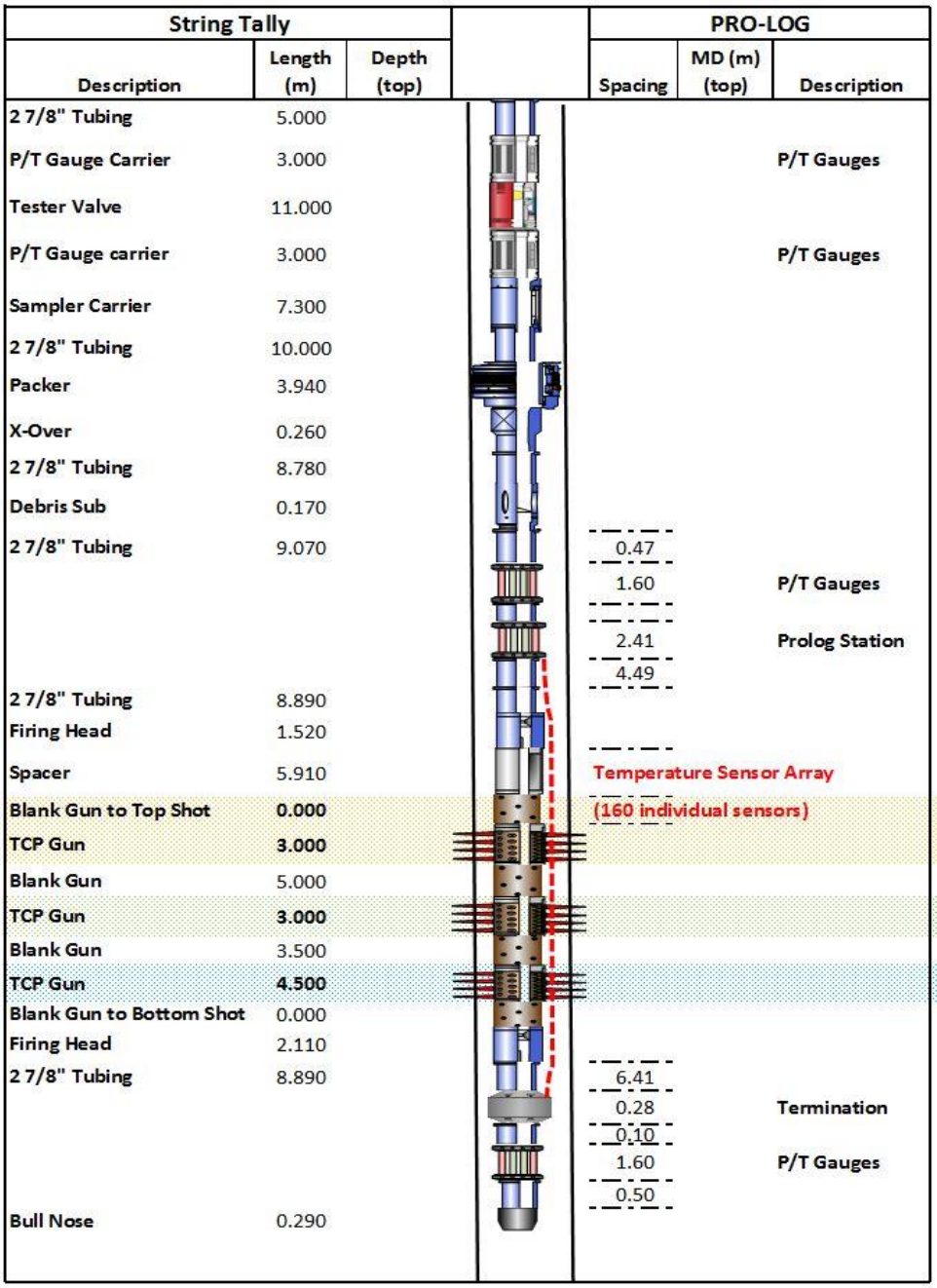

Figure 22- Configuration of the distributed temperature measurement deployment during DSTs.

5.2 Liquid Condensate Behavior Analysis

The first field case data comes from a well drilled, cased, and temporarily plugged, and abandoned many months before testing. Re-opening the well for testing resulted in three days of circulation, which cooled the near-wellbore rock formation by about 0.8 ^{o}C. The well was perforated, and ten days later, a DST string was run across the perforated interval below a packer, as shown in Figure 23. Two discrete temperature sensor arrays were run, clamped to the 3 ½" tubing from 12 m below the bottom of the perforations up to a few meters above the top of the perforations. The spacing of the sensors in each array provided an effective sensor spacing of 0.5 m in this case. Additionally, pressure/temperature gauges were run below, in the middle, above the perforated zone, and in a gauge carrier above the packer but below a tester valve to provide continuous pressure gradients in the wellbore, as shown in Figure 24. Following a short initial flow and build-up, the well flowed for a 24-hour clean-up flow and shut-in for 48 hours.

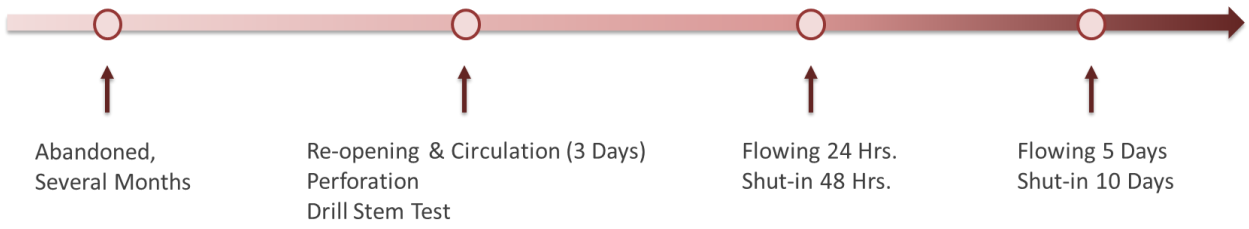

Figure 23- The development timeline of the Field 1.

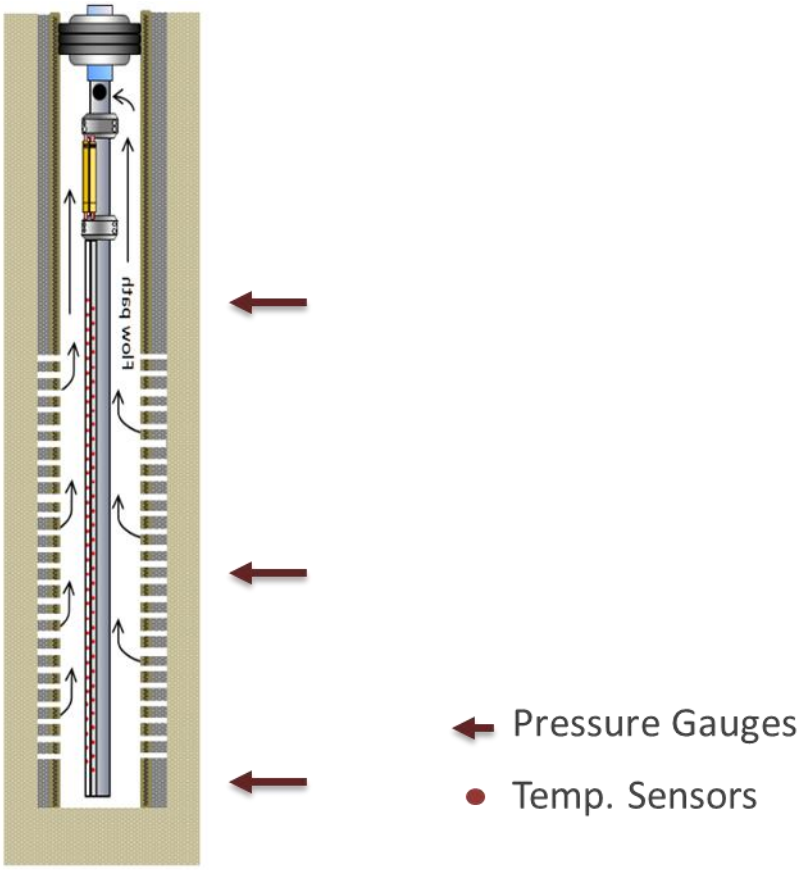

Figure 24- Temperature sensors and pressure gauges installation location.

A three-rate flow followed this after a flow test lasting five days, and the well was then shut-in for ten days. Throughout the test, the wellbore temperature profiles were continuously recorded on the downhole MDTS tools, and the data wirelessly retrieved at the surface. The well was in a gas-condensate reservoir, containing predominantly lighter hydrocarbons (CH_4 and C_2H_6 with some longer chain hydrocarbons, C_3+). The reservoir has a 10-15% porosity with several shaly layers separating sand beds which were a few meters in thickness. At a short distance from the wellbore, the sand beds are well connected. Near the wellbore, the shaly isolating layers allowed the sand beds to behave as individual zones in terms of gas and liquid preferential flow

paths, with sufficient vertical permeability to enable each phase to segregate under the influence of gravity. The gas entry point at x17.00 m is directly under one of these shaly layers.

Figure 25 identifies some of the formation heterogeneities, which help to explain the apparent thermal anomalies. Although the reservoir was a gas-condensate one, the initial estimation was that condensates would not produce from during pressure analysis. The novelty in the temperature data analysis in this field case lies in identifying the phenomenon of J-T heating of liquid condensate coexisting with J-T cooling of lean gas, at different layers in the formation, through their transitory thermal profiles. This is a subtle effect, identified only by continuous monitoring of the changing thermal profiles at high resolution using the recently developed technology.

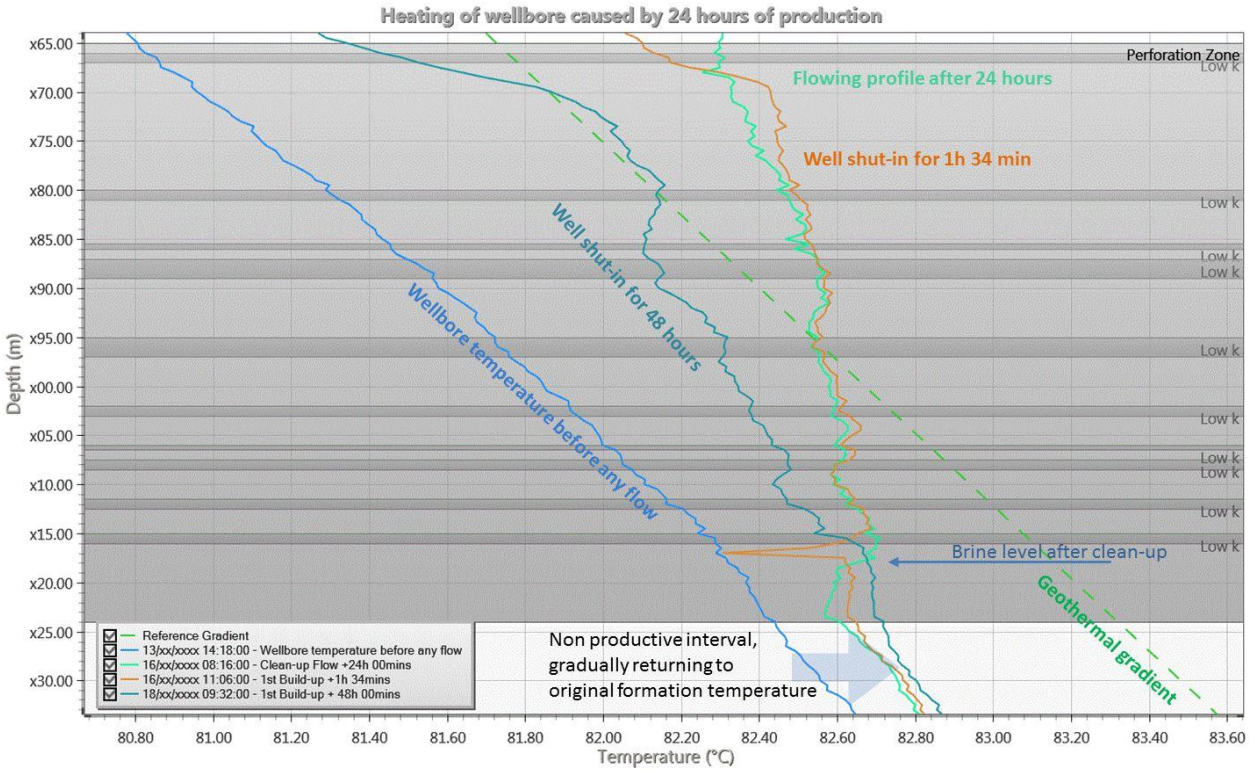

Figure 25- Wellbore temperature profiles at four definitive times.

Because the near-wellbore region was cooled by three days of circulation, initial fluid production was cold when the well was opened to flow, gradually rising towards the undisturbed formation temperature depending on the flow rate and the thermal characteristics of the fluid and the rock. A Horner plot technique was used to calculate the projected temperature at infinite time below the perforated interval, with no fluid movement during the DST.

The first indication that this well was not behaving as an expected dry gas well was the rapidity with which the flowing temperature profile increased towards the geothermal gradient during the 24-hour clean-up flow period. The well was drawn down by 80 psi during the clean-up flow, and the reservoir pressure was 500 psi, below the J-T inversion curve for pure methane; therefore, some J-T cooling of gas would have been expected (calculated about 0.25 ^{o}C). Methane

gas (at pressures below about 7,200 psi), undergoing a pressure drop from the reservoir to the wellbore, expands at constant enthalpy (no heat transferred or work performed) and experiences a temperature reduction. Conversely, liquids (and heavier hydrocarbon gasses) undergoing a similar pressure drop will experience a temperature increase. A mixture of methane and the heavier hydrocarbons has a lowered J-T inversion pressure, but this was a relatively lean gas composition. The J-T inversion pressure of the mixture suggests that there should be a negligible J-T effect for an 80 psi pressure drop. The computation of the J-T coefficient and J-T cooling is described in the Appendix.

Figure 25 shows the wellbore temperature profiles at four definitive times; (1) before flowing the well, (2) warmed up at the end of the 24 hour clean-up flow period, (3) not cooling off after 1 ½ hour of a shut-in, and, (4) after 48 hours of a shut-in. During the flow period, the middle to the upper part of the perforated wellbore was heated by hotter fluid rising from deeper producing intervals (above x05.00 m), obscuring the temperature at which the middle and upper intervals had been producing. On shutting in the well, dry gas-producing intervals naturally should have cooled down to less than geothermal gradient temperature within a few minutes because the near-wellbore rocks have not been heated up enough to go back to undisturbed temperatures. This cooling occurred only at x17.00 m. The pressure gradient showed this depth to be the top of the brine column that had not cleaned up during the flow.

During the 24-hour clean-up flow, the heavier hydrocarbon components dropped out of the gas solution while still in the near-wellbore rock matrix. Because liquid condensate has a considerably greater viscosity than lean gas, the condensate production rate into the wellbore became lower than the rate at which it was being formed further away from the wellbore. Because of the gravity, the liquid condensate coalesced into a bank around the wellbore (on top of each

shaly layer). The more mobile, now-lean gas found a flow path above the condensate layer (underneath the shaly layer). The liquid condensate experienced small but measurable (by MDTS) J-T heating as it flowed towards the wellbore; the lean gas experienced a minimal amount of J-T cooling as it flowed towards the wellbore. When the well was shut in for the first build-up, the cooler gas flow ceased within a few minutes. Still, the hot condensate bank that had developed during the flow slowly collapsed under the influence of gravity, weeping into the wellbore and maintaining that interval of wellbore hotter than geothermal gradient temperature. As the height of the condensate banks in each layer continued to fall over 30 hours of a shut-in, the region of the wellbore wall being maintained hotter than geothermal temperature also descended. Figure 26 illustrates the anomalous temperature behavior over 30 hours of the first shut-in. The thermal effect of the separate phases, confined between two low permeability layers, can be seen. The lean gas had been experiencing a small amount of J-T cooling while flowing over the condensate bank, experiencing J-T heating. The gas entry point at x17.00 m (Figure 26) is directly under one of these shaly layers. Gas condensate reservoirs are characterized by the predominance of lighter hydrocarbons such as CH_4 (60-95%) and C_2H_6 (4-8%) with a proportion of longer chain hydrocarbons (C3+). Gas condensate reservoirs, classified between volatile oil and wet gas reservoirs, will always produce gas mixed with liquid condensate at the surface, with the quantity of condensate varying from reservoir to reservoir. When the flowing bottom hole pressure falls below the dew point pressure, liquid condensate begins to form in the rock formation around the wellbore. Thermodynamically, a gas condensate reservoir is a vapor-liquid equilibrium system

that is a function of temperature, pressure, and fugacity of each component. A change in reservoir pressure or temperature will trigger a difference in the reservoir system thermal energy, leading to the dropout of hydrocarbons from the initial single-phase gas.

Figure 27 is a schematic of the condensate bank's effect in one of the layers collapsing into the wellbore over the 48 hour shut-in period. Most of the intervals between two low permeability layers exhibited similar thermal behavior, characterized by hot spots that slowly descended over the 48 hours of the shut-in. These hot spots were caused by J-T heated liquid condensate weeping into the wellbore, thereby slowing the significant wellbore cooling. As the top of the condensate bank descended throughout the shut-in, the formation above was then able to cool off further. This

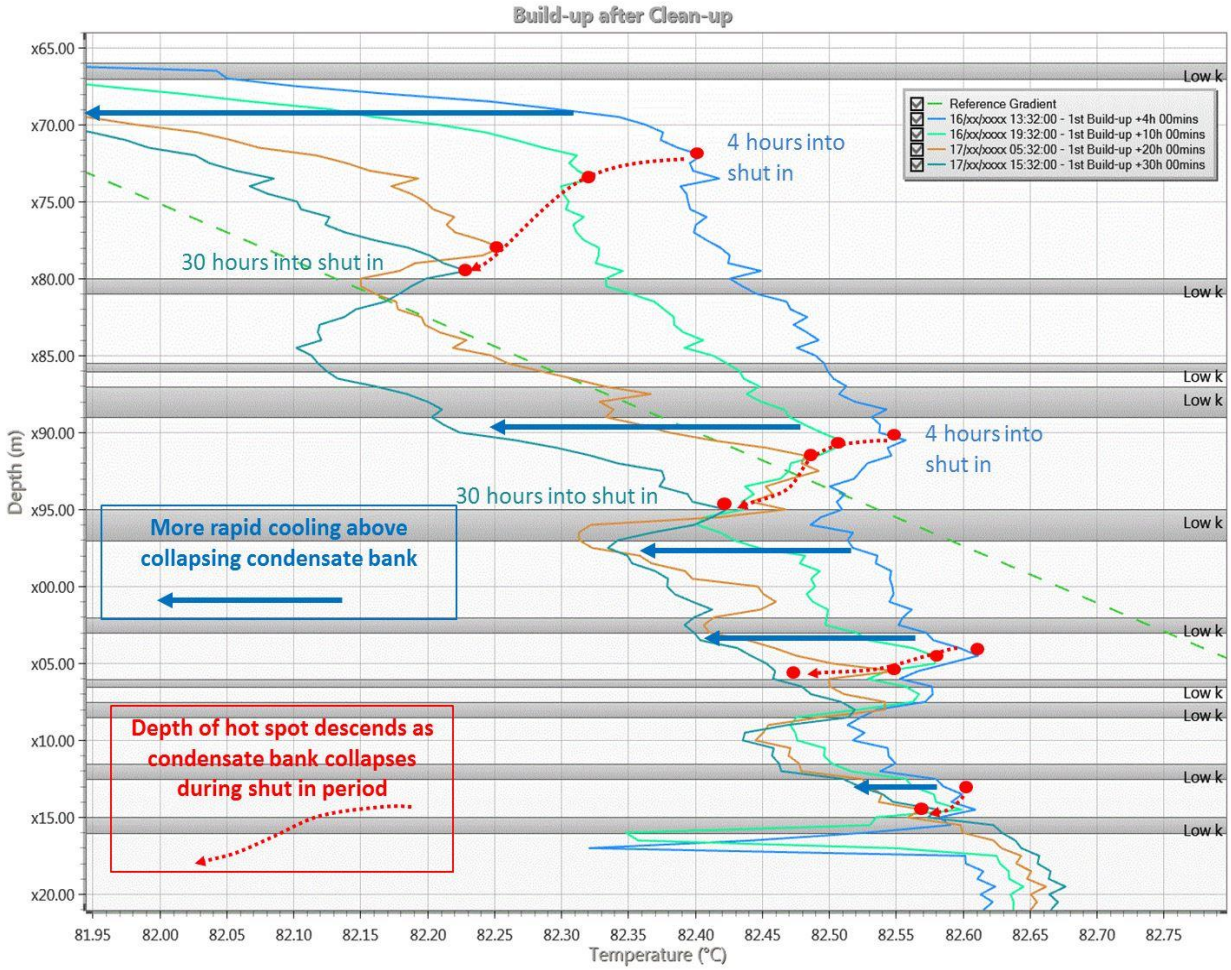

Figure 26- Cooling of wellbore after clean-up flow.

adds to the evidence that the liquid had been heated in the formation during the flow period. A similar effect can be seen at several other producing intervals, creating an unusual rippling down thermal profile during the shut-in.

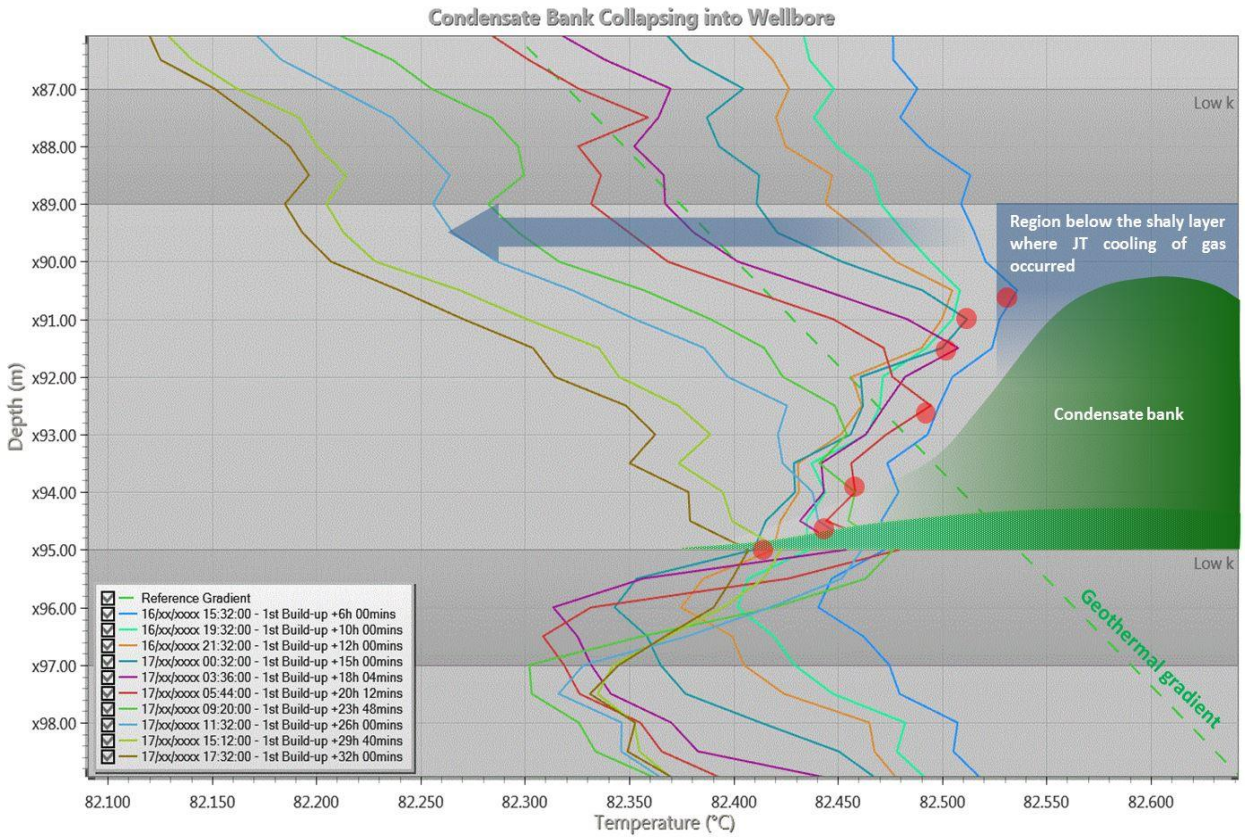

Figure 27- Wellbore thermal profiles in a 6 m deep producing layer indicating cooling behavior. Hot (red) spots, as well as the thermal profiles, are declining with time.

Figure 28 plots the change of pressure gradient between the gauges below the perforations and the mid-perforation gauges (assuming the brine density and depth as constant). As the apparent liquid level, taken from the thermal profiles, passed the mid-perforation gauges, the condensate density was calculated at 0.673 g/cc.

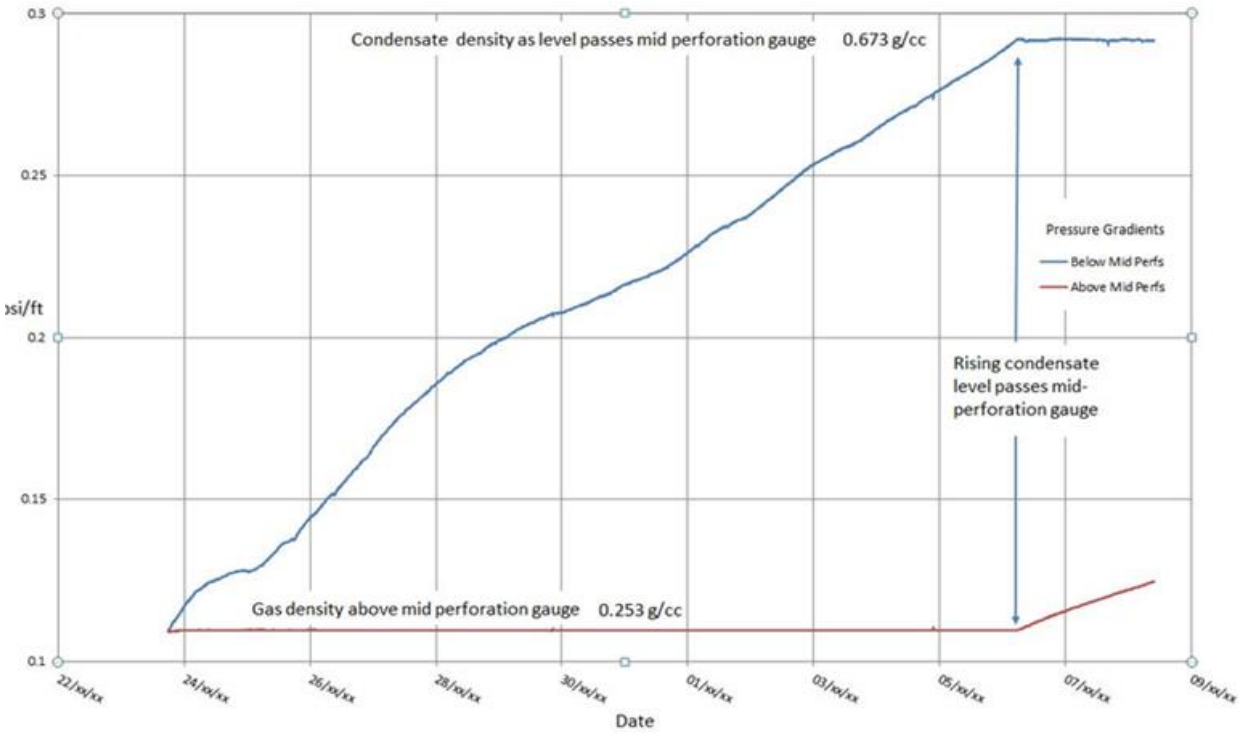

Figure 28- Pressure gradient between the bottom and mid-perforation gauges for the main build-up.

5.3 Identification of Pay-zone Depth

The second example comes from a field that, at the bottom-hole conditions, only produces liquids from the three pay zones. Figure 29 shows these three producing zones with undisturbed formation temperature (broken green line) as well as wellbore fluid temperature just before perforation. Circulation-related cooling of about 14.5 °F, is evidenced in this diagram. Liquids from these three zones, and even within each zone, have different densities and heat capacities in this case. This variation in density and heat capacity complicates zonal allocation computation using the McKinley Mixing Method. Figure 30 shows the schematic of applying the mixing method.

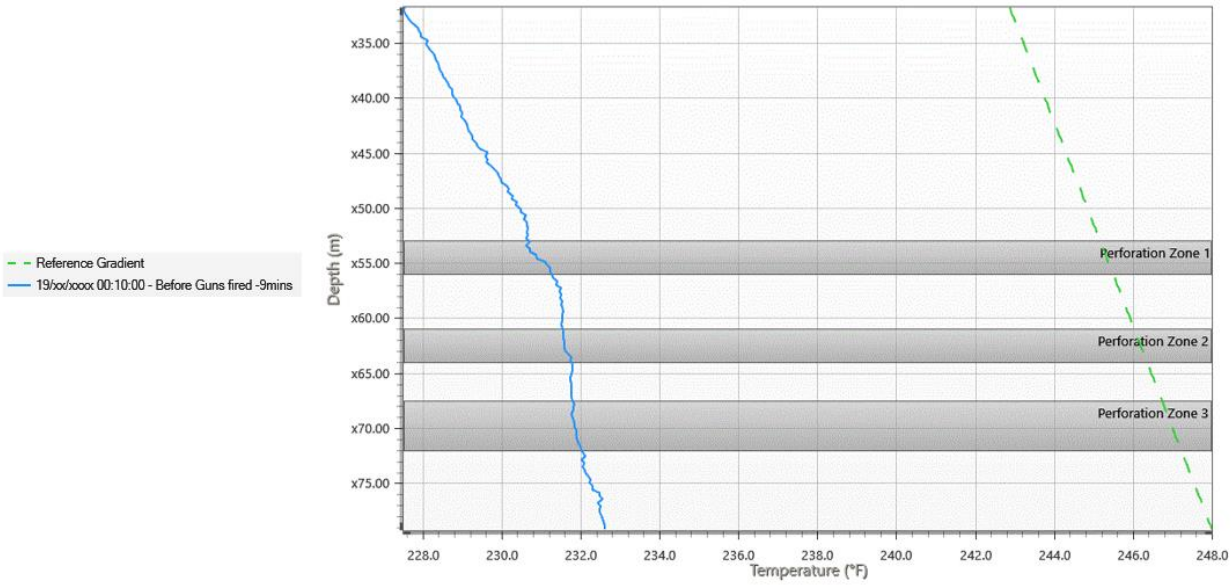

Figure 29- Wellbore temperature before perforating and calculated geothermal gradient.

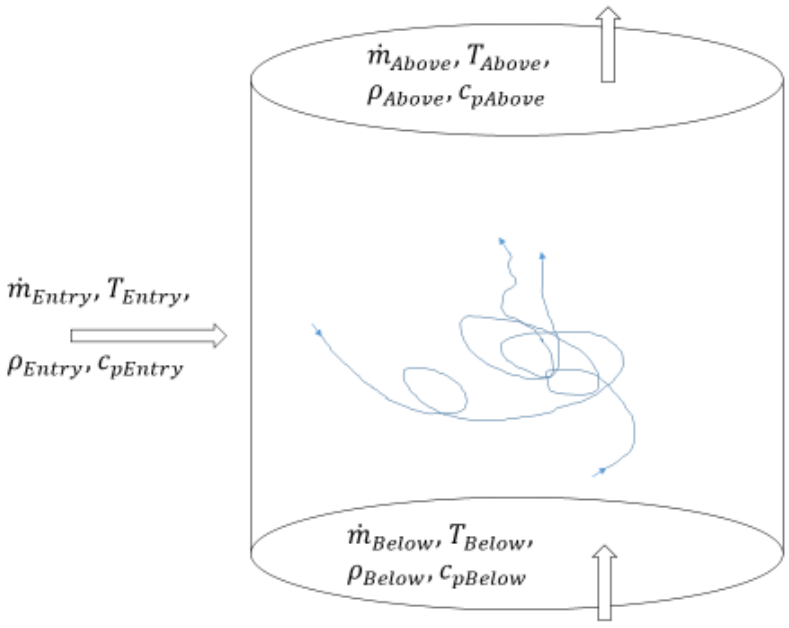

Figure 30- Schematic for Mixing Rule application.

$$\frac{\dot{m}_{Below}}{\dot{m}_{entry}} = \frac{\left(T_{Above}c_{p,Above}\rho_{Above}\right) - \left(T_{Entry}c_{p,Entry}\rho_{Entry}\right)}{\left(T_{Below}c_{p,Below}\rho_{Below}\right) - \left(T_{Entry}c_{p,Entry}\rho_{Entry}\right)} \quad (12)$$

In Eq. 12, $\dot{m}$ represents the mass flow rate, T is the temperature of the fluid, and c_p and ρ are specific heat capacity and density of the fluid, respectively. When properties of the fluid entering from the reservoir are the same as those of the fluid moving up from below, c_p and ρ values in the numerator and denominator are canceled out. That simplifies Eq. 12 to a form generally used in the industry, Eq. 13.

$$\frac{\dot{m}_{Below}}{\dot{m}_{entry}} = \frac{\left(T_{Above}\right) - \left(T_{Entry}\right)}{\left(T_{Below}\right) - \left(T_{Entry}\right)} \quad (13)$$

However, as mentioned earlier, because of significant differences in fluid properties in this system, Eq. 13, without any simplification, must be used for this system. The determination of the wellbore fluid interface (i.e. the interface between the water and oil layer) from the pressure gradients enables the fluids' density to be calculated using simple fluid mechanic techniques. The wireless temperature sensor array data provide accurate fluid interface depths during the build-up periods of the DSTs. Additionally, the pressure gauges placed in the DST string above and below the perforated interval, as shown in Figure 22, confirm interface depths. At the interface between two fluids in the wellbore, the pressure at the interface is equal. Fluid interfaces in the reservoir were determined using a normal hydrostatic pressure regime gradient of 0.45 psi/ft. When the well is shut-in for the main build-up period after the perforating and main flow period, this technique can be used to determine the produced fluids' properties. For two-phase flow, the calculation of

the fluid densities from this method allows the mass flowrate to be adequately attributed to each zone using Eq. 13 and permits a more accurate determination of the J-T effect. For the accurate estimation of related fluid properties and flow information, multiple well flow tests have been conducted. Table 10 offers the parameters of these tests.

Description	Duration
Perforation and Initial Flow	3 hours and 50 minutes
Initial Build-up	42 minutes
Clean-up Flow	25 hours
Build-up after Clean-up Flow	30 hours and 51 minutes
Main Flow – 24/64” choke	8 hours and 29 minutes
Main Flow – 32/64” choke	8 hours and 12 minutes
Main Flow – 40/64” choke	9 hours and 25 minutes
Main Build-up	11 hours and 57 minutes
Bottom Hole Sampling Flow	1 hour and 35 minutes
Shut-in after Sampling Flow	2 hours

Table 10- The information of flow duration for multiple well tests.

During the DST, temperature data allowed an inference that there was a column of higher density liquid periodically building-up in the wellbore. Figure 31 is a plot of temperature data over 5 minutes during the clean-up flow. The red line with arrows in Figure 31 shows that peak-to-peak temperature maintains for about 4.5 minutes.

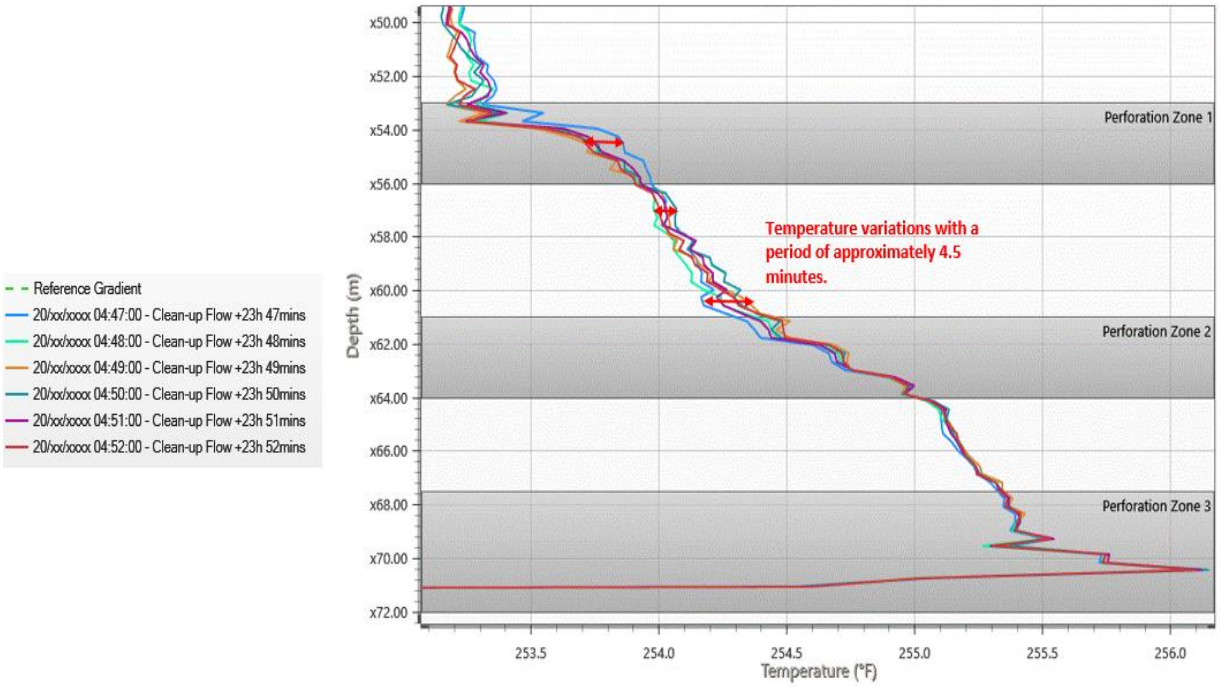

Figure 31- Temperature profiles during the clean-up period.

Figure 33 describes the slugging liquid production from the lower perforated zone. This is also evident in the temperature data plotted for the three pay zones in Figure 31.

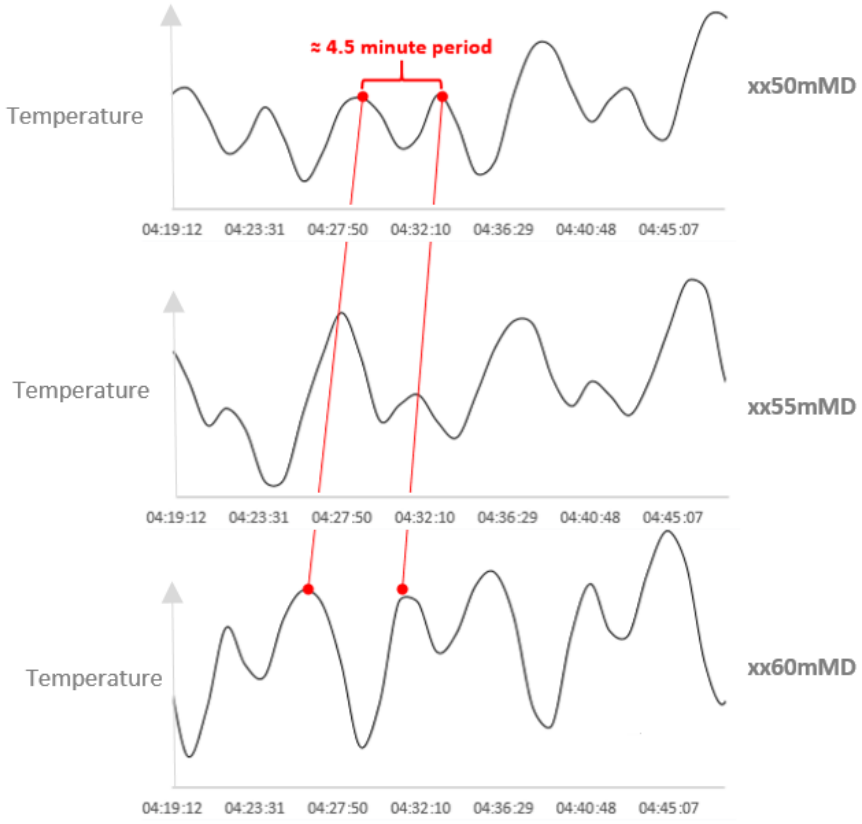

Figure 32- Slugging of hotter fluid noted in the temperature array data.

5.3 Determination of fluid interface and properties.

After cessation of the clean-up flow period, the well was shut-in for around 31 hours, allowing the fluid column in the wellbore to become static. This static fluid begins to cool down, gradually going back to the geothermal temperature. However, the cooling rates for fluids between xx58.18 m and xx58.68 m depths are much slower than those fluids at a shallower depth. This slower cooling rate of deeper zone fluid is attributed to its much higher heat capacity than the shallower depth fluids. Figure 33 highlights the different cooling rates of the various fluids; the temperature sensors below the fluid interface in the build-up periods exhibit a slower cooling rate.

It is reasonable to assume that below this fluid interface at 58.18 m, saline water, with a specific heat value of about 4.2 kJ/kg exists, as shown in Figure 34. Above that interface is the oil with a specific heat of about 2.5 kJ/kg. Due to the sluggish nature of the production from the deepest perforated zone, the interface depth between the produced oil and water was different in each of the shut-in periods.

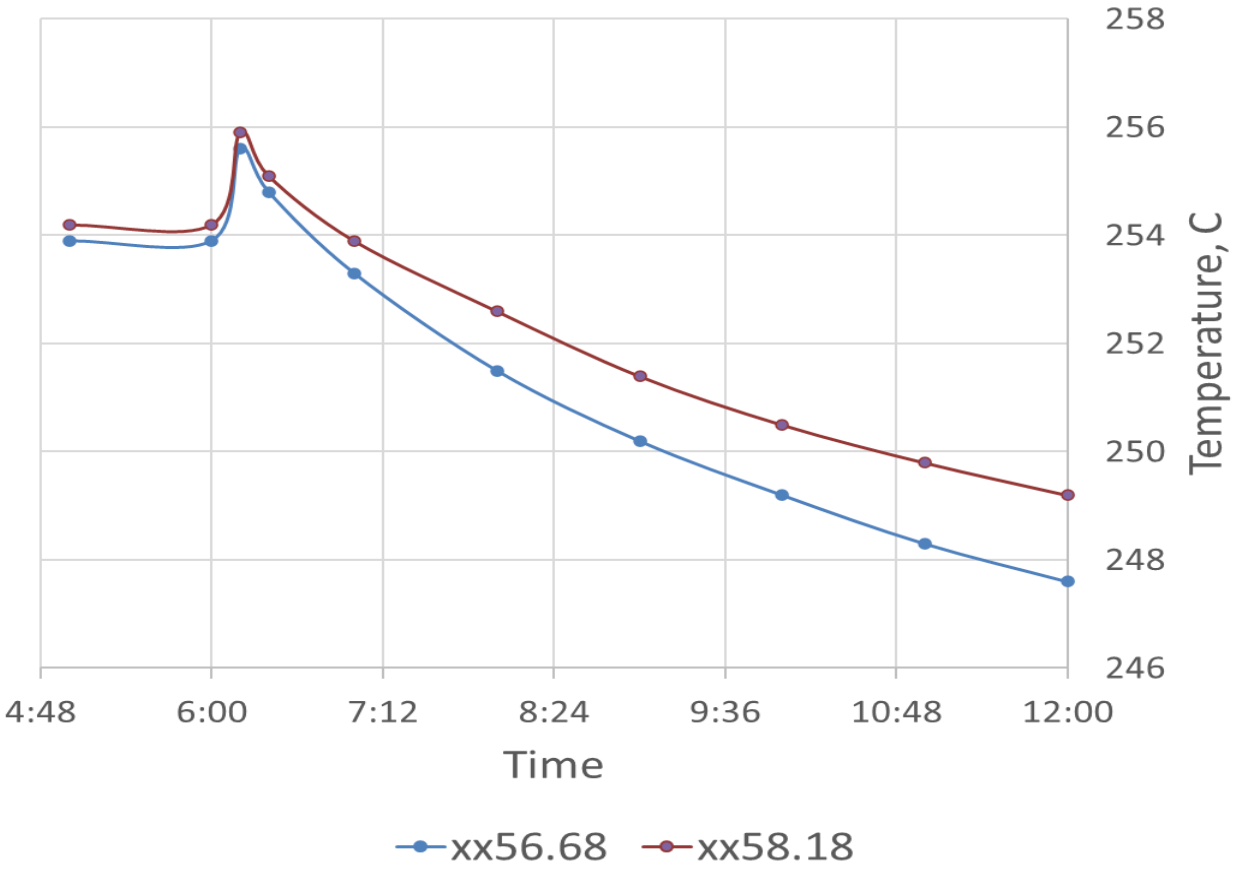

Figure 33- The cooling rate of produced fluids at different depths.

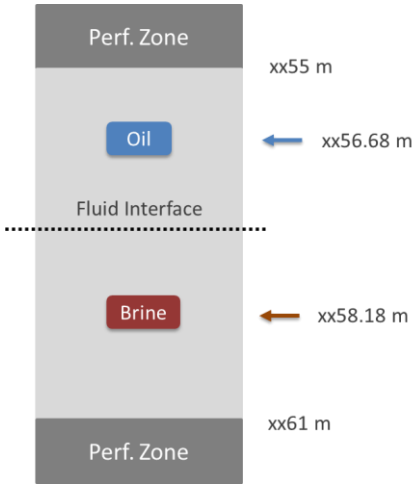

Figure 34- The fluids placement in the payzone.

Without the temperature data, the fluid interfaces would not have been appreciable from the pressure gauge data alone due to the standard gauge configuration (above the test valve, below the test valve, above guns, below guns). As such, the determination of the fluid properties would have higher uncertainty. Figure 35 shows a sequence of temperature profiles during build-up after the clean-up flow period. Because during the build-up, there are no produced fluids to transfer heat from the reservoir to the surface, the wellbore cools off. As the wellbore cools off during the build-up period, the fluid interfaces are easily identified in the temperature data due to the different heat capacities; those with a higher heat capacity tend to stay warmer for longer. Temperature data between perforated zones 1 and 2 clearly show that early build-up time fluid temperatures remain low up to a depth of xx57 m, then increase by about 1 degree for the deeper fluid – clearly indicating the presence of higher thermal capacity (heavier) fluid below. At approximately ten hours into the build-up period, this interface between the denser brine and the oil begins to descend in the wellbore. In this case, the completion fluid remains cool since the formation fluids production has not heated it up at this depth.

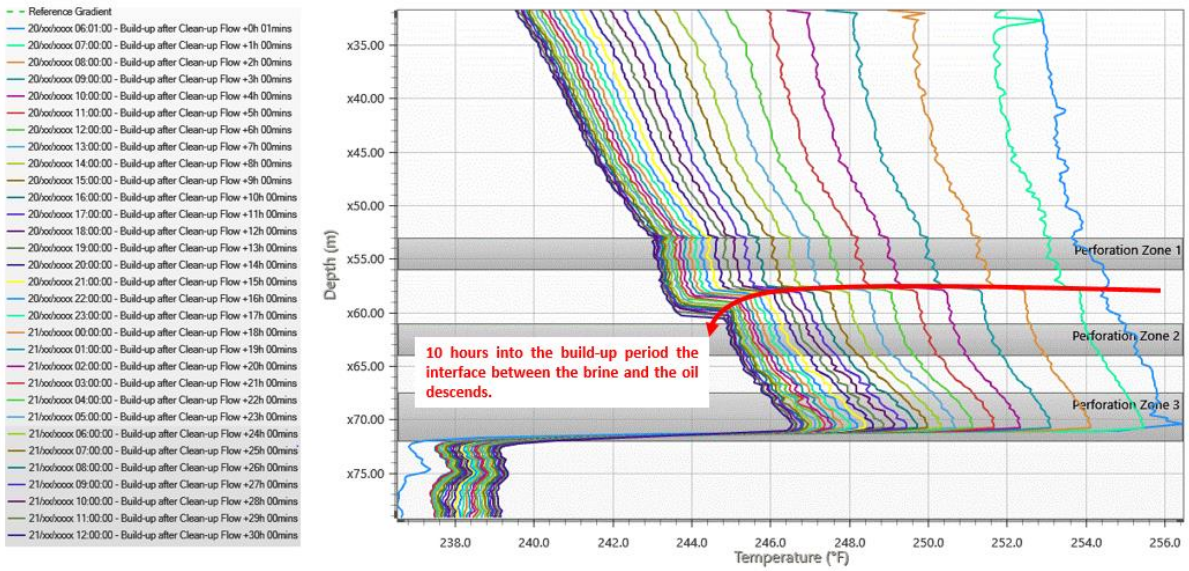

Figure 35- Fluid interface between the brine water and produced hydrocarbon fluid.

Below xx71.5 m measured depth, the temperature remained cool throughout the flowing periods because there was no formation fluid production below this depth. This fluid below the perforations is the original completion fluid. Based on the pressure gradients before perforating, the completion fluid had a density of 1.12 g/cc.

5.4 Accurate Pressure Measurement Using Pressure Gauges

The pressure gradient of the produced oil phase is determined directly from the measured gradient between the pressure gauges below the tester valve and above the perforating guns. Extrapolating this gradient to the fluid interface depth as measured by the temperature array between brine and oil allows the determination of the interface pressure. The completion fluid pressure gradient was extrapolated from the pressure gauge below the perforation guns to the fluid interface level between the denser fluid and the completion fluid. By the pressure and depth information at each of the interfaces, the denser fluid density is calculated. The gradients in Figure

36 show the analysis of the density measurements during the first build-up period. This process was repeated for each of the three build-up periods. Estimation of the fluid properties from the three build-up periods was consistent.

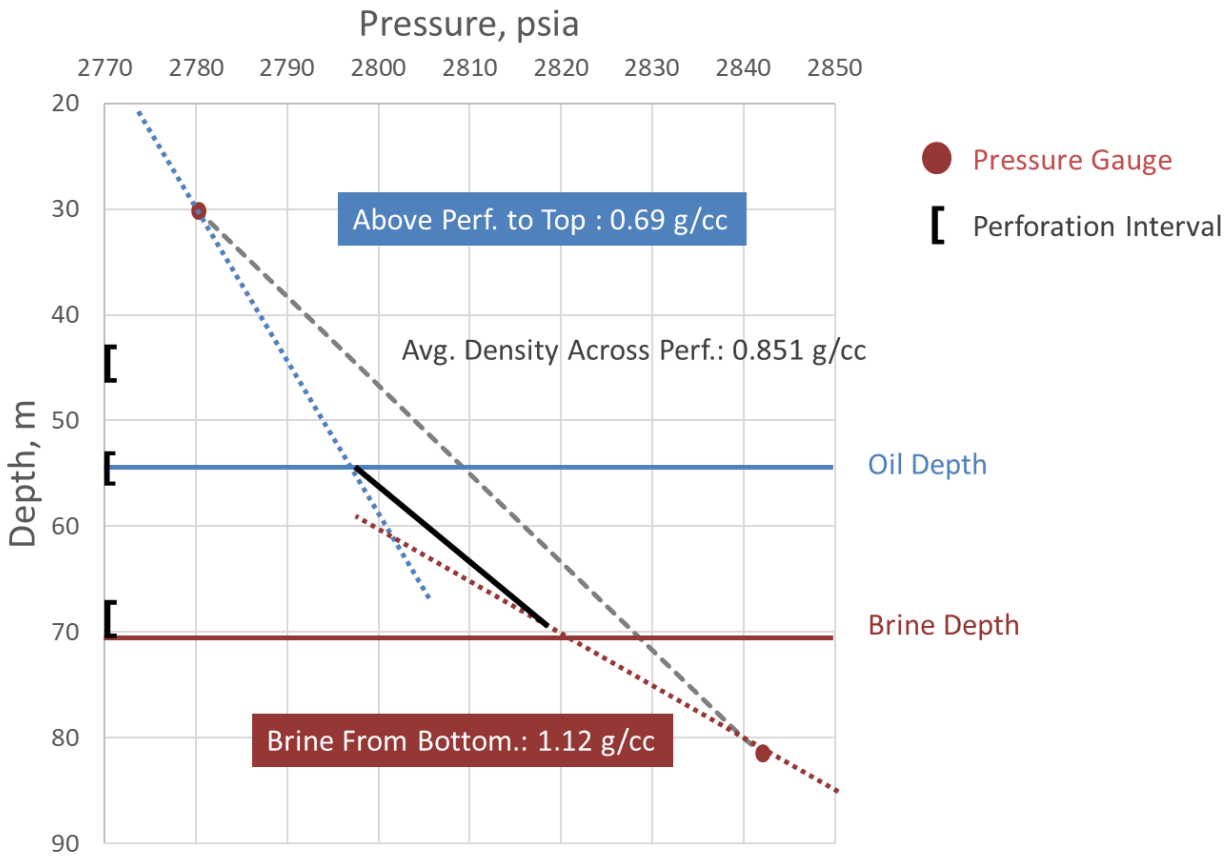

Figure 36- Temperature profile at the end of the first choke setting of the main flow period.

5.5 Improved Zonal Contributions Calculation

As mentioned earlier, the zonal inflow contributions were estimated from the mass enthalpy method, Eq. 13, taking into account the differences in the fluid density and heat capacity. Knowledge of the main contributing intervals increases the robustness of the mass enthalpy

method for determining the zonal contributions because accurate density and heat capacity values are available. Figure 37 shows the percentage contribution of each zone based on the changing fluid properties (black bar). This is compared to the flowrates where the fluid properties were not considered, and only the temperature difference was used (grey bar). When the fluid properties are not fully considered, the deepest perforated intervals appear to produce double the actual water production and correspondingly less overall oil production from the upper two perforated intervals.

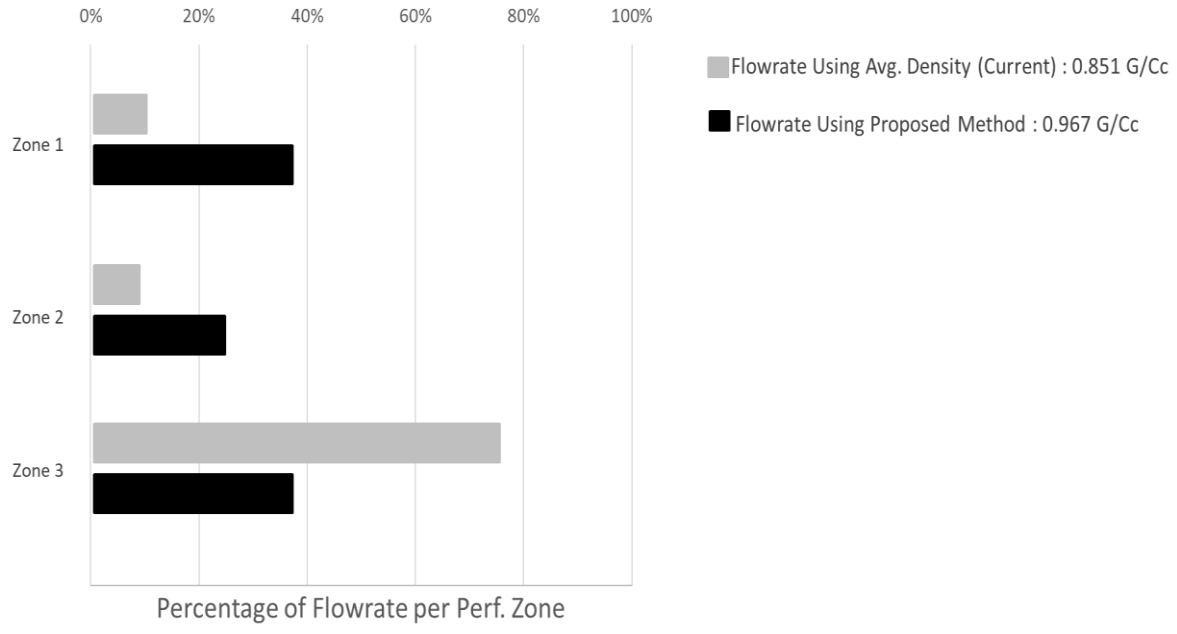

Figure 37- Flowrate contribution for each perforated interval during the main flow period's first choke setting.

6. STEADY-STATE HEAT TRANSFER IN A RESERVOIR SYSTEM

6.1 Model Development

The reservoir system is approximated as a single-phase fluid flowing from the reservoir boundary toward the wellbore in 1-D radial coordinates, as shown in Figure 38. The underlying assumptions in the model are:

1. Oil is the only flowing fluid in the reservoir (i.e. no free gas) and flows at a constant rate.
2. The fluid temperature (T_{ei}) and pressure (P_{ei}) in the reservoir are constant at the reservoir boundary (r_e).
3. All reservoir properties, such as porosity and permeability, are constant throughout the flow period.
4. The density and viscosity of the fluid in the reservoir are constant.

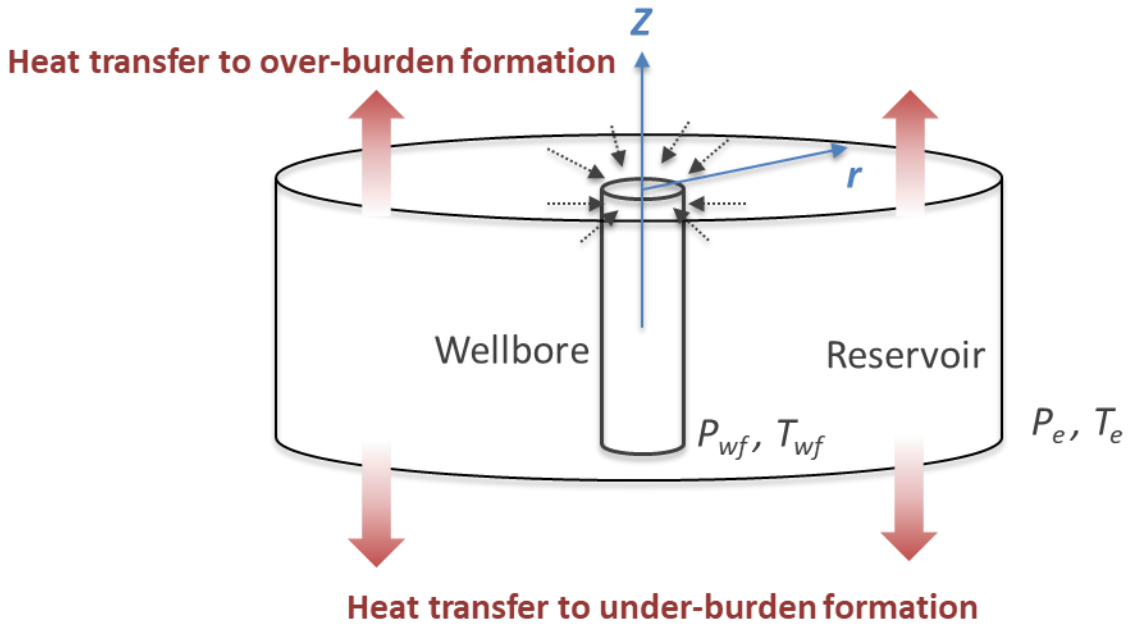

Figure 38- Schematic of the wellbore/reservoir formation.

The comprehensive energy-balance equation for this system can be reduced to this partial-differential equation:

$$\left[\emptyset s_f \rho_f c_{pf} + \emptyset s_w \rho_w c_{pw} + (1-\emptyset)\rho_e c_{pe}\right]\frac{\partial T}{\partial t} + \rho_f u_r c_{pf}\frac{\partial T}{\partial r} + \rho_f u_r \sigma_f \frac{\partial p}{\partial r} + \left[\emptyset s_f \rho_f \sigma_f + \emptyset s_w \rho_w \sigma_w - 1\right]\frac{\partial p}{\partial t} = \frac{1}{r}\frac{\partial}{\partial r}\left(\lambda r \frac{\partial T}{\partial r}\right) \quad (14)$$

In Eq. 14, subscripts *f*, *w*, and *e* refer to the fluid (oil), water, and earth (formation), respectively. The first and fourth terms on the left side are time-dependent, and because steady-state is assumed, they can be omitted, and since oil is the only fluid in the system, the subscript *f* can be replaced by *o* (oil), yielding Eq. 15.

$$\rho_o u_r c_{po} \frac{\partial T}{\partial r} + \rho_o u_r \sigma_o \frac{\partial P}{\partial r} = \frac{1}{r} \frac{\partial}{\partial r} \left(\lambda r \frac{\partial T}{\partial r} \right) \tag{15}$$

Eq. 15 is the comprehensive energy-balance equation for this system. The terms on the left side of Eq. 15 represent convection and energy change due to the J-T effect. The term on the right describes the change in energy from radial heat conduction. The local velocity of the fluid can be obtained from Darcy's equation and a detailed derivation is presented in Appendix B. The energy-balance equation can be reduced to the following second-order ordinary differential equation.

$$\frac{d^2 T}{dr^2} + A \frac{1}{r} \frac{dT}{dr} + B \frac{1}{r^2} = 0 \tag{16}$$

The two BCs are (1) the initial temperature at the outer reservoir boundary and (2) thermal insulation at the wellbore wall.

$$T(r_e) = T_{ei} \tag{17}$$

$$\left(\frac{\partial T}{\partial r} \right) = 0 \ \ at \ \ r = r_w \tag{18}$$

The final form of the proposed analytical solution is

$$T(r) = T_{ei} + \frac{B r_w^{1-A} \left(r_e^{1-A} - r^{1-A} \right)}{(A-1)^2} + \frac{B}{A-1} \ln \left(\frac{r_e}{r} \right) \tag{19}$$

where,

$$A = \left(\frac{2\pi h \lambda + \rho_o q c_{po}}{2\pi h \lambda} \right) \tag{20}$$

$$B = \left(\frac{\mu q^2 \rho_o \sigma_o}{(2\pi h)^2 k \lambda} \right) \tag{21}$$

6.2 Model Validation

We compared our model with the analytical solution by App and Yoshikawa (2013) for validation. Table 11 presents the parameters of the reservoir and fluid generated by App and Yoshikawa's (2013) model.

WELL, FORMATION, AND FLUID DATA	
Reservoir boundary, ft	5,325
Wellbore radius, ft	0.35
Pay-zone height, ft	10
Porosity	0.18
Permeability, md	20
Fluid thermal conductivity, Btu/hr-°F-ft	1.93
Fluid density, lb_m/ft^3	25
Fluid specific heat capacity, Btu/lb_m-°F	0.53
Fluid viscosity, cp	1
J-T coefficient, °F/psi	0.0059
Formation volume factor, bbl/STB	1.05
Initial reservoir temperature, °F	250
Initial reservoir pressure, psi	10,000

Table 11- Well, formation, and fluid data for validation.

Figure 39 shows the comparison result: the solid blue and red lines represent the radial temperature distribution estimated by App and Yoshikawa and our model, respectively. The proposed model shows the same result as App and Yoshikawa's solution, where the temperature difference between the two models is less than 0.1% throughout the radial distance range from the wellbore.

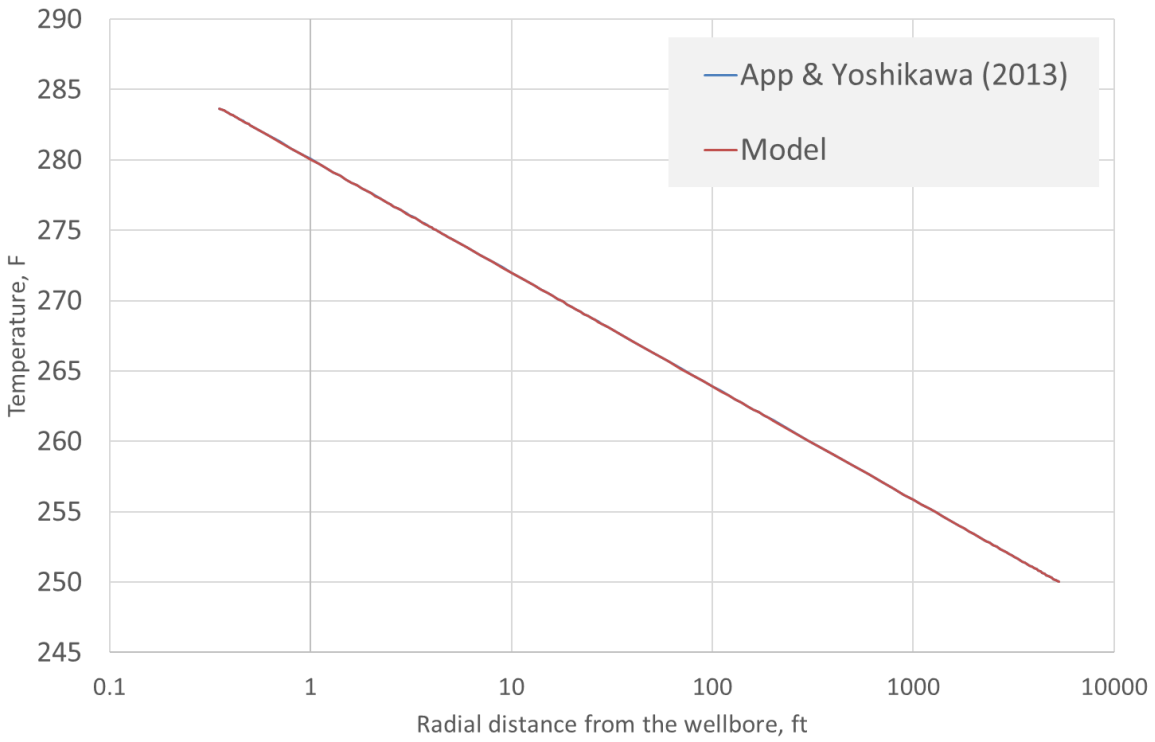

Figure 39- Comparison of the radial temperature distribution between the two models.

6.3 Effect of System Heat Transfer

The reservoir is non-isothermal during the production period due to a combination of several heat transfer mechanisms. The most influential mechanism is the J-T effect (Steffensen and Smith, 1973; App, 2010; Xu et al., 2018; Chevarunotai et al., 2018). Due to the J-T heating in the oil well, the fluid temperature in the reservoir rises as it flows, and almost reaches the maximum value where the fluids exit to the wellbore. Other than the J-T effect, adiabatic expansion and heat transfer from the reservoir to the over-burden and the under-burden formations is the representative mechanism that should be considered when estimating the temperature. Xu et al. (2018) reported that the effect of adiabatic expansion is negligible compared with that of the heat exchange with

over- and under-burden formations. Therefore, adiabatic expansion is not taken into account in this thesis.

Chevarunotai et al. (2018) investigated heat transfer from a reservoir to over- and under-burden formations resulting in radial temperature distribution. The reservoir fluids lose heat while ascending to the surface after entering the wellbore, which means energy is transferred from the system (reservoir fluids and formation) to the surroundings (over- and under-burden formations). We define this heat transfer across the system boundary as "system heat transfer" for clarity in this thesis. The system heat transfer is related to the surrounding formation in a complex manner; therefore, Chevarunotai et al. (2018) approximated this term using Newton's law of cooling, giving

$$\dot{\mathrm{Q}} = -\frac{2\mathrm{h_c}(\mathrm{T} - \mathrm{T_s})}{h_c} \tag{22}$$

where subscript *s* represents the surrounding and h_c is the heat transfer coefficient. Chevarunotai et al. (2018) observed a large temperature difference when considering the system heat transfer in a high-drawdown oil reservoir. They reported a maximum of 10 °F temperature difference when applied to the well data from App (2010).

Here we present the analysis when the system heat transfer Chevarunotai's transient analytical solution for the system heat transfer is modified into the steady-state condition. The transient solution is (Chevarunotai et al., 2018):

$$T(r,t) = T_i + \frac{C}{2B} e^{\left(\frac{HAr^2+2Bt}{2B}\right)} Ei\left(-\frac{HAr^2+2Bt}{2B}\right) - \frac{C}{2B} e^{\left(\frac{HAr^2}{2B}\right)} Ei\left(-\frac{HAr^2}{2B}\right) \tag{23}$$

Let substitute n,

$$\frac{H(Ar^2 + 2Bt)}{2B} = n \tag{24}$$

The exponential integral part can be rewritten as follows:

$$\lim_{n\to\infty} e^n \, Ei(-n) = \lim_{n\to\infty} \frac{Ei(-n)}{e^{-n}} \tag{25}$$

Implementing the L'Hopital's formula, the exponential integral part changes,

$$\lim_{n\to\infty} \frac{\frac{d}{dn}(Ei(-n))}{\frac{d}{dn}(e^{-n})} = \lim_{n\to\infty} \frac{-\frac{e^{-n}}{n}}{-e^{-n}} = \lim_{n\to\infty} \frac{1}{n} = 0 \tag{26}$$

Therefore, the second term on the side of the transient solution is omitted. The steady-state solution is:

$$T(r) = T_i - \frac{C}{2B} e^{\left(\frac{HAr^2}{2B}\right)} Ei\left(-\frac{HAr^2}{2B}\right) \tag{27}$$

where,

$$A = \left[\phi s_f \rho_f c_{pf} + \phi s_w \rho_w c_{pw} + (1-\phi)\rho_e c_{pe}\right]\left(\frac{2\pi h}{q}\right) \tag{28}$$

$$B = \rho_f c_{pf} \tag{29}$$

$$C = \frac{q\rho_f \sigma_f \mu_f}{2\pi h k} \tag{30}$$

$$D = \frac{4h_c \pi}{q} \tag{31}$$

$$H = \frac{D}{A} \tag{32}$$

The results from Chevarunotai's and the proposed model to identify the system heat transfer effects are shown in Figure 40. The logarithmic radial distance from the wellbore is plotted on the x-axis. The gray line represents the proposed model, the blue line Chevarunotai's model, and the red line Chevarunotai's model without system heat transfer using the same reservoir and fluid heat properties in Table 11. The flow rate in this comparison is 181.4 STB/d, and the Peclet number at this rate is 10.

Figure 40- Comparison of the radial temperature distribution between models to identify the system heat transfer effect.

The wellbore wall temperature (T_w) at 0.35 ft is higher than that at the reservoir boundary at 5,325 ft in all three cases due to J-T heating. The proposed model shows a radial temperature difference of about 7.5 °F and the result of Chevarunotai's model without system heat transfer is

almost the same. However, Chevarunotai's model including the system heat transfer shows a radial temperature difference about 2.5 °F, which is lower than the two cases mentioned above. This smaller temperature difference arises from the system heat transfer caused by heat loss to the flowing fluids, reducing the temperature throughout the whole radial distance range.

Another difference between Chevrunotai's model and this model is that there exists a certain radial distance where the temperature converges to the undisturbed formation temperature (T_{ei}). This radial distance was defined as the thermally affected radius (r_a) in chapter 4. r_a is much smaller than the reservoir boundary in Chevarunotai's model regardless of the inclusion of system heat transfer. The significantly short r_a is a characteristic of the functions that make up their solution, which will be discussed further later. Chevarunotai's model is still utilized for identifying the system heat transfer effect despite the temperature convergence phenomenon. The proposed model is used to estimate the temperature when the system heat transfer is not included.

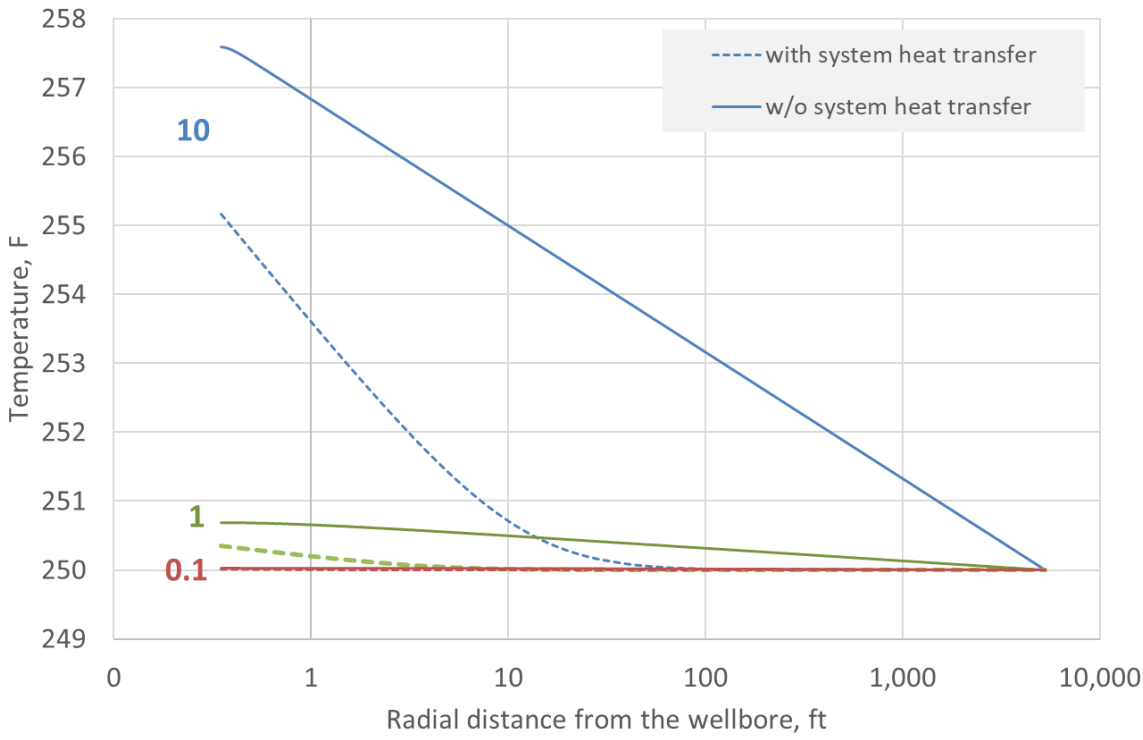

Figure 41- The radial temperature at different Peclet numbers compared with those from modified Chevarunotai's (2018) model.

Figure 41 shows the system heat transfer effect with varying Peclet numbers. All solid lines in Figure 41 indicate the cases not including the system heat transfer while the dashed lines do. The Peclet numbers are 0.1, 1, and 10 with corresponding flow rates of 1.81, 18.1, and 181.4 STB/d, respectively. When the Peclet number is either 0.1 or 1, the system heat transfer effect is minimal since the T_w difference between the solid and dashed lines is very small (in the case of Peclet number = 0.1, it is negligible). However, when Peclet number is 10, the effect becomes noticeable as is evidenced by a T_w difference of ca. 2.5 F.

$$\text{Pe} = \frac{ur}{\alpha} = \frac{q\rho c_p}{2\pi h\lambda} = \frac{k\Delta p}{\alpha\mu \ln\left(\frac{r_e}{r_w}\right)} \tag{33}$$

The system heat transfer is induced when there is a temperature difference in the reservoir, as shown in Eq. 22. This means that the system heat transfer is dependent on the temperature difference due to the J-T effect (heating in the oil reservoir). The relationship between Peclet number and other parameters implementing Darcy's law is described in Eq. 33. The Peclet number is proportional to the pressure drawdown, which means a larger Peclet number induces more J-T heating in the reservoir. Although the system heat transfer leads to a lower reservoir temperature, contrary to J-T heating, its effect is proportional to that of J-T.

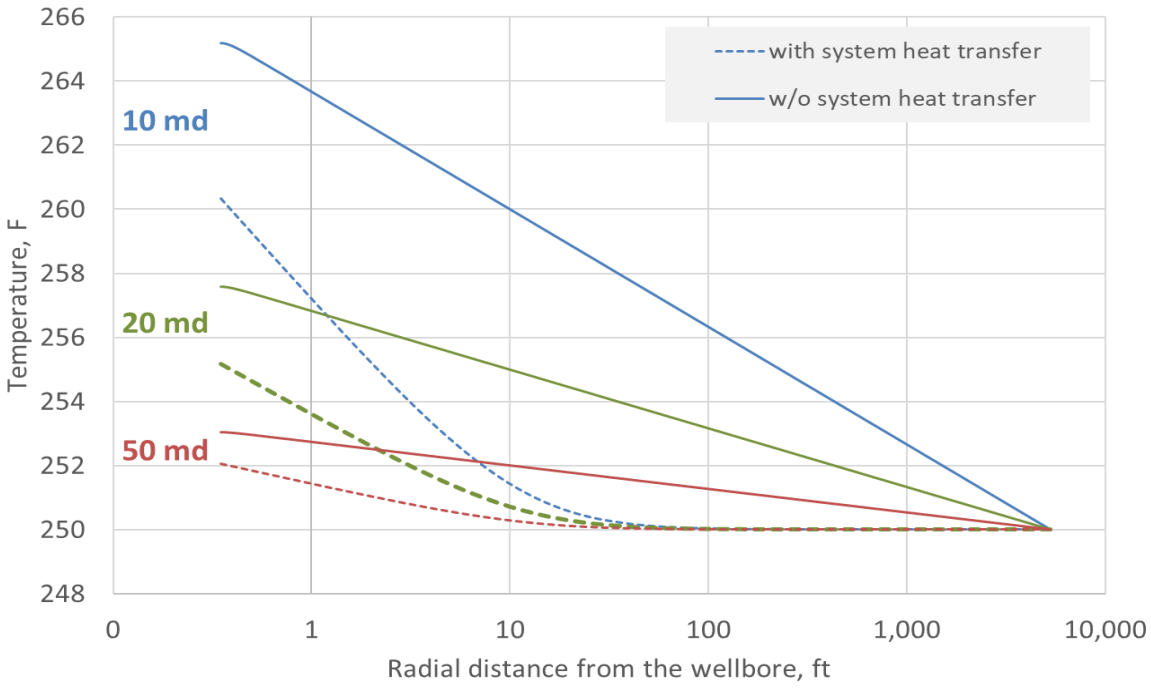

Figure 42- The radial temperature at different permeabilities compared with those from modified Chevarunotai's (2018) model.

Figure 42 shows the system heat transfer effect under a constant Peclet number of 10 with different permeabilities. The dashed and solid lines for each color correspond to the results with and without system heat transfer, as in Figure 41, for each permeability value. Figure 42 shows

the tendency that lower permeability leads to a larger system heat transfer. This can be explained by the fact that the lower permeability requires more pressure drop in the reservoir to produce the same flow rates. As before, the system heat transfer effect is confirmed to occur in proportion to the J-T effect which relies on the pressure drop.

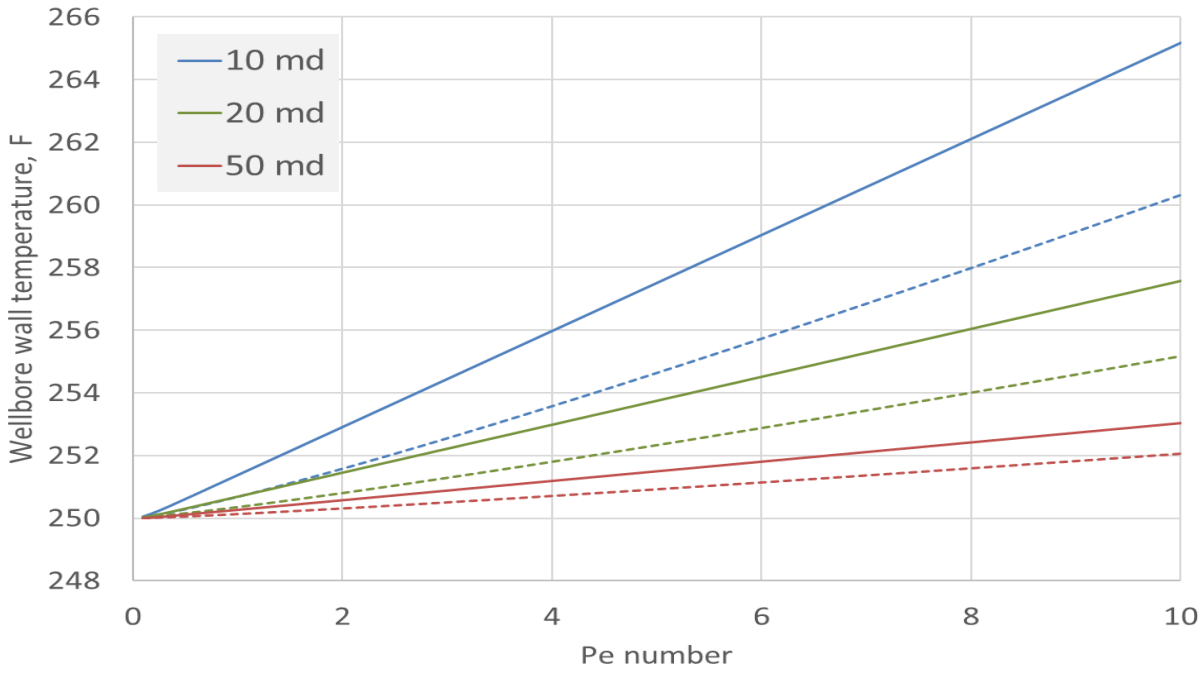

Figure 43- Wellbore wall temperature with Peclet number at different permeabilities compared with those from modified Chevarunotai's (2018).

Figure 43 is a comparison of T_w according to Peclet number at different permeabilities. T_w increases as the Peclet number increases because a larger Peclet number leads to an increased pressure drop, inducing more J-T heating. A larger Peclet number also triggers the system heat transfer, indicated by the temperature difference between the solid and dashed lines of each color, as shown in Figure 43. Lower permeability causes a larger system heat transfer, and the same trend is observed in Figure 42. Note the system heat transfer contributes about 5 °F in the case

when the permeability is 10 md and the Peclet number is 10. In this context, tight oil reservoirs typically have very low permeabilities, some of which are even below 0.1 md. T_w can be much higher than T_{ei} under certain operating conditions, so the temperature difference between T_w and T_{ei} must be considered in reservoirs with very low permeabilities for safe and cost-effective design of fluids and operational facilities.

6.4 Discussions

Chevarunotai's model consistently converges to T_{ei} at a certain radial distance. The steady-state condition signified an infinite flow period and that heat diffusion is complete. This means temperature differences at any radial distance should exist even if the radial distance is far from the wellbore. As Chevarunotai et al. (2018) discussed, their model estimates the radial temperature distribution within a short flow period due to the characteristics of the exponential integral (Ei) function. A component in their solution converges to zero when the input value is less than -1. The Ei function output is valid only for a very limited range of values, and Figure 44 illustrates the output according to the radial distance in the current system. The Ei function output begins to converge at a radial distance of about 10 ft and converges to zero above 100 ft**.** The radial distance in which the temperature converges to T_{ei} matches Chevarunotai's result (solid blue line) in Figure 40.

Chevarunotai's model has enough estimation capacity in the real reservoir even with the fact that it is difficult to apply the steady-state condition. The thermal diffusivity of the formation is typically very small compared to its hydraulic diffusivity, and an extremely long period can be required to end transient heat diffusion. The maximum target period for production is often

estimated to be about 30 years, but only a few years for commercial-purposed production are available in unconventional reservoirs. However, their model still results in meaningful estimation given the steady increase in unconventional reservoirs.

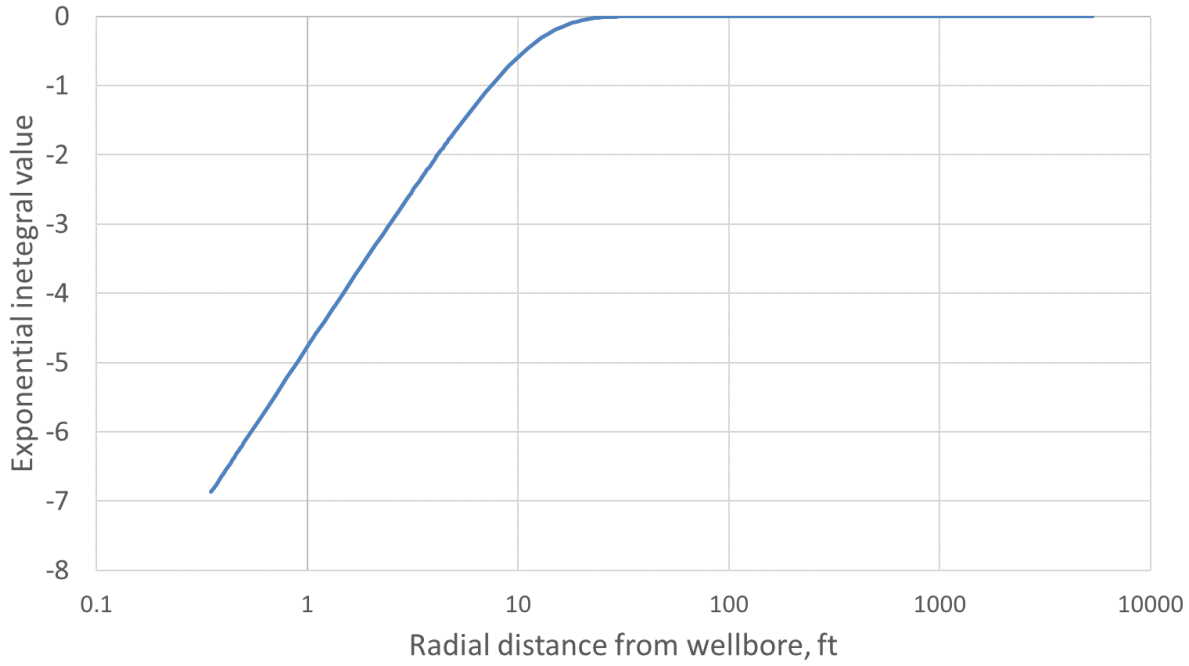

Figure 44- Ei function value as a function of radial distance from the wellbore.

7. SUMMARY AND CONCLUSIONS

This dissertation presents an approach to study heat transfer during drilling, completion, and production periods.

The conclusions for jet pump operation are:

1. The proposed analytical model predicts fluid temperature profiles in both conduits, tubing, and annulus. This model is versatile and easily implemented to counter-current flow systems other than jet pumps.
2. The temperature difference between the tubing and annulus is not large because the heat capacity of the injection fluid is generally much larger than that of the reservoir fluid, and the thermal resistance between the tubing and the annulus is small.
3. Both injection rate and temperature are essential in determining the frictional pressure gradient for safe and effective production design, with the injection rate having more significant influence.
4. The proposed numerical iteration method enables identifying the entire temperature profile in the wellbore and only needs the temperature data at the surface. This saves the time and cost required for measuring the subsurface temperatures.

The near-wellbore cooling quantification conclusions are:

1. Heat exchange between the circulated drilling fluid and the formation causes the near-wellbore cooling effect. The developed analytic model effectively describes the radial temperature profile and its influence.

2. The influence of flow rate on the extent of the thermally affected radius is minimal but circulation time significantly influences the radius.

The newly developed MDTS provides us with ultra-high resolution temperature data continuously; it gives us many potential applications.

1. The temperature profile across the producing interval indicates liquid condensate forming within the reservoir and collapsing while moving to the wellbore. It also recognizes the separate flow paths of leaner gases and liquid condensates within each permeable layer in the heterogeneous reservoir.
2. The MDTS data enables us to determine the interface depth of liquids with different properties, leading to a more accurate estimation of liquid density. Thus, it provides the potential to calculate the zonal flow rate contributions and the pressure profiles with higher accuracy. A standard DST with only downhole pressure gauges would not have detected such differentiation.

The non-isothermal fluid behavior in the reservoir system results in the following conclusions:

1. The heat exchange with the over- and under-burden formations (defined as the system heat transfer in this thesis) influences the reservoir temperature even at steady-state.
2. The system heat transfer effect is proportional to the Peclet number and the flow rate but has an inverse correlation with the permeability.

3. The system heat transfer effect can be maximized in tight oil reservoirs with very low permeabilities; this heat transfer mechanism is an essential component in estimating the reservoir temperature accurately.

REFERENCES

Al Saedi, A. Q., Flori, R. E., & Kabir, C. S. (2019). Exploring alteration of near-wellbore geothermal gradient during fluid circulation and production. *Journal of Petroleum Science and Engineering*, *177*, 909-920.

App, J. F. (2010). Nonisothermal and productivity behavior of high-pressure reservoirs. *Spe Journal*, *15*(01), 50-63.

App, J., & Yoshioka, K. (2013). Impact of reservoir permeability on flowing sandface temperatures: dimensionless analysis. *Spe Journal*, *18*(04), 685-694.

Alves, I. N., Alhanati, F. J. S., & Shoham, O. (1992). A unified model for predicting flowing temperature distribution in wellbores and pipelines. *SPE production Engineering*, *7*(04), 363-367.

Beirute, R. M. (1991). A circulating and shut-in well-temperature-profile simulator. *Journal of Petroleum Technology*, *43*(09), 1-140.

Chevarunotai, N., Hasan, A. R., Kabir, C. S., & Islam, R. (2018). Transient flowing-fluid temperature modeling in reservoirs with large drawdowns. *Journal of Petroleum Exploration and Production Technology*, *8*(3), 799-811.

Chew, J. N., & Connally Jr, C. A. (1959). A viscosity correlation for gas-saturated crude oils. *Transactions of the AIME*, *216*(01), 23-25.

Christou, K., Fyfe, D., & Hasan, A. R. (2019). Using High Resolution Temperature Data in Appraisal Wells to Identify the Reservoir Conditions that can Lead to Condensate Blockage. *Offshore Mediterranean Conference and Exhibition*. Offshore Mediterranean Conference.

Danielsen, P. E. (2008). High temperature geothermal logging for temperature and pressure. In *Conference, ARGeo C-2, Entebbe, Uganda*.

Dranchuk, P. M., Purvis, R. A., & Robinson, D. B. (1973). Computer calculation of natural gas compressibility factors using the Standing and Katz correlation. *Annual Technical Meeting*. Petroleum Society of Canada.

Edwardson, M. J., Girner, H. M., Parkison, H. R., Williams, C. D., & Matthews, C. S. (1962). Calculation of formation temperature disturbances caused by mud circulation. *Journal of Petroleum Technology*, *14*(04), 416-426.

Eppelbaum, L. V., & Kutasov, I. M. (2006). Pressure and temperature drawdown well testing: similarities and differences. *Journal of Geophysics and engineering*, *3*(1), 12-20.

Espinosa-Paredes, G., Garcia, A., Santoyo, E., & Hernandez, I. (2001). TEMLOPI/V. 2: a computer program for estimation of fully transient temperatures in geothermal wells during circulation and shut-in. *Computers & geosciences*, *27*(3), 327-344.

Fan, J., Eves, J., Thompson, H. M., Toropov, V. V., Kapur, N., Copley, D., & Mincher, A. (2011). Computational fluid dynamic analysis and design optimization of jet pumps. *Computers & Fluids*, *46*(1), 212-217.

Gao, Y., Sun, B., Xu, B., Wu, X., Chen, Y., Zhao, X., & Chen, L. (2017). A wellbore/formation-coupled heat-transfer model in deepwater drilling and its application in the prediction of hydrate-reservoir dissociation. *SPE journal*, *22*(03), 756-766.

Hamedi, H., Rashidi, F., & Khamehchi, E. (2011). Numerical prediction of temperature profile during gas lifting. *Petroleum science and technology*, *29*(13), 1305-1316.

Hasan, A. R., & Kabir, C. S. (2012). Wellbore heat-transfer modeling and applications. *Journal of Petroleum Science and Engineering*, *86*, 127-136.

Hasan, A. R., & Kabir, C. S. (1996). A mechanistic model for computing fluid temperature profiles in gas-lift wells. *SPE Production & Facilities*, *11*(03), 179-185.

Hasan, A.R., and Kabir, C.S., 2018. Fluid flow and heat transfer in wellbores. 2nd edition. Richardson, Texas: Society of Petroleum Engineers.

Hasan, A. R., & Kabir, C. S. (1994). Static reservoir temperature determination from transient data after mud circulation. *SPE Drilling and Completion*, *9*(1).

Hasan, A. R., Kabir, C. S., & Wang, X. (2009). A robust steady-state model for flowing-fluid temperature in complex wells. *SPE Production & Operations*, *24*(02), 269-276.

Hashmi, G. M., Kabir, C. S., & Hasan, A. R. (2016). Design and interpretation of transient tests at well's inception. *Journal of petroleum science and engineering*, *145*, 573-584.

Holmes, C. S., & Swift, S. C. (1970). Calculation of circulating mud temperatures. *Journal of Petroleum Technology*, *22*(06), 670-674.

Hossain, M. S., Sarica, C., Zhang, H. Q., Rhyne, L., & Greenhill, K. L. (2005). Assessment and development of heavy oil viscosity correlations. *SPE International Thermal Operations and Heavy Oil Symposium*. Society of Petroleum Engineers.

Jang, M., & Hasan, A. R. (2020). Countercurrent Flow of Heat in Tubing and Annulus System: Jet Pump. *Offshore Technology Conference Asia*. Offshore Technology Conference.

Ji, D., Zhang, M., Xu, T., Wang, K., Li, P., & Ju, F. (2015). Experimental and numerical studies of the jet tube based on venturi effect. *Vacuum*, *111*, 25-31.

Kabir, C. S., Hasan, A. R., Kouba, G. E., & Ameen, M. (1996). Determining circulating fluid temperature in drilling, workover, and well control operations. *SPE Drilling & Completion*, *11*(02), 74-79.

Kabir, C. S., Yi, X., Jakymec, M., & Hasan, A. R. (2014). Interpreting distributed-temperature measurements in deepwater gas-well testing: estimation of static and dynamic thermal gradients, and flow rates. *SPE Production & Operations*, *29*(02), 97-104.

Kosmicki, R. & Pugh, T. (2017). Jet Pumps Improve Bakken Shale Economy. Hart Energy. Retrieved from http://hartenergy.com.

Kutasov, I. M. (1987). Dimensionless temperature, cumulative heat flow and heat flow rate for a well with a constant bore-face temperature. *Geothermics*, *16*(5-6), 467-472.

Hermanrud, C., Lerche, I., & Meisingset, K. K. (1991). Determination of virgin rock temperature from drillstem tests. *Journal of Petroleum Technology*, 43(09), 1-126.

Lauwerier, H. A. (1955). The transport of heat in an oil layer caused by the injection of hot fluid. *Applied Scientific Research*, Section A, 5(2-3), 145-150.

Lavery, D., Fyfe, D., & Hasan, A. R. (2019). Determining Produced Fluid Properties for Accurate Production Profiling During a Drill Stem Test Using Thermal Imaging Technology. *Offshore Technology Conference Brasil*. Offshore Technology Conference.

Luheshi, M. N. (1983). Estimation of formation temperature from borehole measurements. *Geophysical Journal International*, *74*(3), 747-776. Mahdiani, M. R., & Khamehchi, E. (2016). A novel model for predicting the temperature profile in gas lift wells. *Petroleum*, *2*(4), 408-414.

Mao, Y., & Zeidouni, M. (2017, May). Analytical solutions for temperature transient analysis and near wellbore damaged zone characterization. In *SPE Reservoir Characterisation and Simulation Conference and Exhibition*. Society of Petroleum Engineers.

Mao, Y., & Zeidouni, M. (2018). Accounting for fluid-property variations in temperature-transient analysis. *SPE Journal*, *23*(03), 868-884.

Mu, L., Zhang, Q., Li, Q., & Zeng, F. (2018). A Comparison of Thermal Models for Temperature Profiles in Gas-Lift Wells. *Energies*, *11*(3), 489.

Ouyang, L. B., & Belanger, D. (2004). Flow profiling via distributed temperature sensor (DTS) system-expectation and reality. *SPE Annual Technical Conference and Exhibition*. Society of Petroleum Engineers.

Ramazanov, A. S., Nagimov, V. M., & Akhmetov, R. K. (2013). Analytical model of temperature prediction for a given production history. *Oil and Gas Business*, 1, 537-546.

Ramey Jr, H. J. (1962). Wellbore heat transmission. *Journal of petroleum Technology*, *14*(04), 427-435.

Rubinshtein, L. I. (1959). The total heat losses in injection of a hot liquid into a stratum. *Neft'i Gaz*, 2(9), 41-48.

Sagar, R., Doty, D. R., & Schmidt, Z. (1991). Predicting temperature profiles in a flowing well. *SPE production engineering*, *6*(04), 441-448.

Santoyo, E., Garcia, A., Espinosa, G., Hernández, I., & Santoyo, S. (2000). STATIC_TEMP: a useful computer code for calculating static formation temperatures in geothermal wells. *Computers & Geosciences*, *26*(2), 201-217.

Satman, A., Brigham, W. E., & Zolotukhin, A. B. (1979). A new approach for predicting the thermal behavior in porous media during fluid injection. *Geotherm Resour Counc Trans*, 3, 621-624.

Satter, A. (1965). Heat losses during flow of steam down a wellbore. *Journal of Petroleum technology*, *17*(07), 845-851.

Sayed, M. A., & Al-Muntasheri, G. A. (2016). Mitigation of the effects of condensate banking: a critical review. *SPE Production & Operations*, *31*(02), 85-102.

Shah, A., Chughtai, I. R., & Inayat, M. H. (2011). Experimental and numerical analysis of steam jet pump. *International journal of multiphase flow*, *37*(10), 1305-1314.

Shiu, K. C., & Beggs, H. D. (1980). Predicting temperatures in flowing oil wells.

Spillette, A. G. (1965). Heat transfer during hot fluid injection into an oil reservoir. *Journal of Canadian Petroleum Technology*, 4(04), 213-218.

Steffensen, R. J., & Smith, R. C. (1973, January). The importance of Joule-Thomson heating (or cooling) in temperature log interpretation. In Fall Meeting of the *Society of Petroleum Engineers of AIME*. Society of Petroleum Engineers.

Takacs, G. (2011). How to improve poor system efficiencies of ESP installations controlled by surface chokes. *Journal of Petroleum Exploration and Production Technology*, *1*(2-4), 89-97.

Vargas, A. F., Duran, J., Simpson, A., Santos, R., Doval, J. M., Muñoz, L., ... & Rios, D. (2018, August). Getting wells back to production using an innovative artificial lift system for recovering inactive wells. *SPE Artificial Lift Conference and Exhibition-Americas*. Society of Petroleum Engineers.

Walzel, B. (2019). Decisions Abound in Artificial Lift. Hart Energy. Retrieved from http://hartenergy.com.

Wang, X., Bussear, T. R., & Hasan, A. R. (2010). Technique to improve flow profiling using distributed-temperature sensors. *SPE Latin American and Caribbean Petroleum Engineering Conference*. Society of Petroleum Engineers.

Xu, B., Jang, M., Fyfe, D., & Hasan, A. R. (2020a). Clean-up period flow rate estimation from Multi Discrete Temperature Sensor data. *Journal of Petroleum Science and Engineering*, 107452.

Xu, B., Kabir, C. S., & Hasan, A. R. (2018). Nonisothermal reservoir/wellbore flow modeling in gas reservoirs. *Journal of Natural Gas Science and Engineering*, *57*, 89-99.

Xu, B., Tang, H., Fyfe, D., & Hasan, A. R. (2020b). Analytical modelling of temperature profiles during deepwater drilling operation. *Journal of Petroleum Science and Engineering*, *184*, 106582.

Yang, M., Tang, D., Chen, Y., Li, G., Zhang, X., & Meng, Y. (2019a). Determining initial formation temperature considering radial temperature gradient and axial thermal conduction of the wellbore fluid. *Applied Thermal Engineering*, *147*, 876-885.

Yang, M., Luo, D., Chen, Y., Li, G., Tang, D., & Meng, Y. (2019b). Establishing a practical method to accurately determine and manage wellbore thermal behavior in high-temperature drilling. *Applied Energy*, *238*, 1471-1483.

Yu, Y., & Li, K. (2013). A method for calculating the temperature profile in heavy oil wells with the injection of light oil diluent. *Petroleum science and technology*, *31*(24), 2569-2576.

APPENDIX A: ANALYTIC SOLUTION OF HEAT TRANSFER IN THE COUNTER-CURRENT FLOW

ODE derivation of Hasan and Kabir (1996) to jet pumps

This section presents the derivation process of applying Hasan and Kabir's counter-current flow heat transfer model to a jet pump. We use the depth coordinate, *z*, to be positive in the downward direction. In the tubing, $Q_t(z)$ amount of heat enters the element by convection at depth *z*, and $Q_t\ (z+dz)$ heat leaves the element by convection at depth $z+dz$. In addition, Q_{ta} amount of heat flow from the annulus to the tubing. Mathematically,

$$w_t Q_t(z+dz) = w_t Q_t(z) + Q_{ta} dz$$

or,

$$\frac{dQ_t}{\mathrm{d}z} = \frac{Q_{ta}}{w_t} \tag{A-1}$$

In the annulus, $Q_a(z+dz)$ heat enters the element by convection, and Q_F heat flows from the formation by conduction. In addition, $Qa(z)$ heat leaves the annulus by convection, and Q_{ta} heat flows from the annulus to the tubing. Thus,

$$w_a Q_a(z+dz) + (Q_F - Q_{ta})\mathrm{d}z = w_a Q_a(z)$$

or,

$$\frac{dQ_a}{\mathrm{d}z} = \frac{(Q_{ta} - Q_F)}{w_a} \tag{A-2}$$

The wellbore formation interface temperature is related to the annular fluid temperature by the annulus overall heat transfer coefficient for annulus, U_a, in terms of the casing outer radius, r_{co}, as follows,

$$Q_F = 2\pi r_{co} U_a (T_{ei} - T_a) \tag{A-3}$$

Heat transfer Q_F, between the formation and the annulus fluid, is given by (Hasan et al., 1996) the following expression,

$$Q_F = w_a c_{p,a} L_R (T_{ei} - T_a) \tag{A-4}$$

where

$$L_R = \frac{2\pi}{C_{p,a} w_a} \left[\frac{r_{co} U_a \mathrm{k}_e}{k_e + r_{co} U_a T_D} \right]$$

Heat transfer, Q_{ta}, between the annular fluid to the power fluid in the tubing is given by:

$$Q_{ta} = 2\pi r_t U_t (T_a - T_t)$$

or,

$$Q_{ta} = \frac{w_a c_{p,a}}{B} (T_a - T_t) \tag{A-5}$$

where

$$B = \frac{w_a c_{p,a}}{2\pi r_t U_t}$$

In the following, we replace Q_a by expressing in terms of temperature only (excluding J-T effect), so that $Q_a = c_{p,a} T_a$. Therefore, in Eq. 2, (dQ_a/dz) becomes $c_{pa}(dT_a/dz)$, and $(Q_F - Q_{ta})$ becomes $(w_a c_{p,a})$ $[L_R (T_{ei} - T_a) - (T_a - T_t)]$. Hence, Eq. 2 is then rewritten as follows,

$$\frac{dT_a}{\mathrm{d}z} = -L_R (T_{ei} - T_a) + \frac{T_a - T_t}{B} \tag{A-6}$$

Similarly, Eq. 1 can be rewritten, using $(dQ_t/dz) = c_{p,t}(dT_t/dz)$, and $Q_{ta} = (2\pi r_t U_t)(T_a - T_t)$, hence

$$T_a = T_t + \frac{w_t c_{p,t}}{2\pi r_t U_t}\frac{dT_t}{dz} = T_t + B_1\frac{dT_t}{dz} \quad \text{(A-7)}$$

where,

$$B_1 = \frac{w_t c_{p,t}}{2\pi r_t U_t}$$

We desire to obtain a single differential equation for tubing fluid temperature, T_t. To do that, Eq. 7 is differentiated to obtain,

$$\frac{dT_a}{dz} = \frac{dT_t}{dz} + B_1\frac{d^2T_t}{dz^2} \quad T_a = T_t + \frac{w_t c_{p,t}}{2\pi r_t U_t}\frac{dT_t}{dz} = T_t + B_1\frac{dT_t}{dz} \quad \text{(A-8)}$$

Replacing the first term (dT_a/dz), in the above Eq. 8 by Eq. 6,

$$-L_R(T_{ei} - T_a) + \frac{T_a - T_t}{B} = \frac{dT_t}{dz} + B'\frac{d^2T_t}{dz^2}$$

Or

$$-(T_{ei} - T_a) + \frac{T_a - T_t}{L_R B} = \frac{1}{L_R}\frac{dT_t}{dz} + \frac{B'}{L_R}\frac{d^2T_t}{dz^2} \quad \text{(A-9)}$$

All the T_a are replaced by Eq. 7,

$$\frac{1}{L_R}\frac{dT_t}{dz} + \frac{B_1}{L_R}\frac{d^2T_t}{dz^2} = -T_{ei} + \left(T_t + B_1\frac{dT_t}{dz}\right)\left(1 + \frac{1}{BL_R}\right) - \frac{T_t}{BL_R} \quad \text{(A-10)}$$

The last term (T_t/BL_R), is canceled out with the 2nd the last term. This leaves

$$\frac{1}{L_R}\frac{dT_t}{dz} + \frac{B_1}{L_R}\frac{d^2T_t}{dz^2} = -T_{ei} + T_t + B_1\frac{dT_t}{dz} + \frac{B_1}{BL_R}\frac{dT_t}{dz} \quad \text{(A-11)}$$

Collecting all the coefficient of the first derivative and using $T_{ei} = T_{eiwh} + g_G z$

$$B_2 \frac{dT_t}{dz} + \frac{B_1}{L_R}\frac{d^2T_t}{dz^2} = T_t - T_{eiwh} - g_G z$$

Rearranging,

$$\frac{B_1}{L_R}\frac{d^2T_t}{dz^2} + B_2 \frac{dT_t}{dz} - T_t + T_{eiwh} + g_G z = 0 \quad \text{(A-12)}$$

where,

$$B_2 = \frac{1}{L_R} - B_1 - \frac{B_1}{BL_R}$$

Overall heat transfer coefficient of the tube and annulus, U_t and U_a are given by,

$$U_t = \left(R_t + \frac{1}{h_t}\frac{r_{ti}}{r_{to}} + \frac{1}{h_a}\frac{r_{to}}{r_{ci}}\right)^{-1} \quad \text{(A-13)}$$

$$U_a = \left(R_{csg} + R_{cem} + \frac{1}{h_a}\frac{r_{to}}{r_{ci}}\right)^{-1} \quad \text{(A-14)}$$

ODE solution

Recalling the final ODE form, Eq. A-12, we simplify the coefficient of the second derivative term, we denote

$$AB_1\frac{d^2T}{dz^2} + B_2 \frac{dT}{dz} - T_t + T_{eiwh} + g_G z = 0 \quad \text{(A-15)}$$

where,

$$A = \frac{1}{L_R}.$$

The homogeneous solution can be obtained as follows:

$$T = e^{\lambda z}, \qquad \frac{dT}{dz} = \lambda e^{\lambda z}, \qquad \frac{d^2T}{dz^2} = \lambda^2 e^{\lambda z} \tag{A-16}$$

Substituting Eq. A-16 into Eq. A-15 and arranging:

$$\begin{gathered} AB_1\left(\lambda^2 e^{\lambda z}\right) + B_2\left(\lambda e^{\lambda z}\right) - e^{\lambda z} = 0 \\ e^{\lambda z}(AB_1\lambda^2 + B_2\lambda - 1) = 0. \end{gathered} \tag{A-17}$$

The characteristic poly-nominal equation for the complementary solution becomes,

$$p(\lambda) = AB_1\lambda^2 + B_2\lambda - 1 = 0 \tag{A-18}$$

The two roots of the complementary solutions are:

$$\begin{aligned} \lambda_1 &= \frac{-B_2 + \sqrt{B_2^2 + 4AB_1}}{2AB_1} \\ \lambda_2 &= \frac{-B_2 - \sqrt{B_2^2 + 4AB_1}}{2AB_1} \end{aligned} \tag{A-19}$$

The discriminant is bigger than zero, then the general solution, T_h, of the related homogeneous equation is:

$$B_2^2 + 4AB_1 > 0 \tag{A-20}$$

$$T_h = \alpha e^{\lambda_1 z} + \beta e^{\lambda_2 z}. \tag{A-21}$$

The particular solution of the Eq. A-12 is as follows:

$$T_p = K_1 z \ + K_0\,, \qquad \frac{dT_p}{dz} = K_1, \qquad \frac{d^2T_p}{dz^2} = \ 0 \tag{A-22}$$

Using Eq. A-22 into Eq. A-15, we obtain,

$$B_2K_1 - (K_1 z + \ K_0) + g_G z \ + T_{eiwh} \ = \ 0$$

$$K_0 = B_2 g_G + T_{eiwh}, \qquad K_1 = g_G \tag{A-23}$$

The particular solution is

$$T_p = g_G z \ \ + B_2 g_G + T_{eiwh}. \tag{A-24}$$

The complete general solution, obtained by adding the particular and the complementary solutions, is

$$T_t = T_h + T_p = \alpha e^{\lambda_1 z} + \beta e^{\lambda_2 z} + g_G z + B_2 g_G + T_{eiwh} \tag{A-25}$$

And

$$T_a = T_t + B_1 \frac{dT_t}{dz}$$

$$= (1 + \lambda_1 B_1)\alpha e^{\lambda_1 z} + (1 + \lambda_2 B_1)\beta e^{\lambda_2 z} + g_G(B_2 + B_1) + g_G z + T_{eiwh} \tag{A-26}$$

BC and constants for tubing-injection model

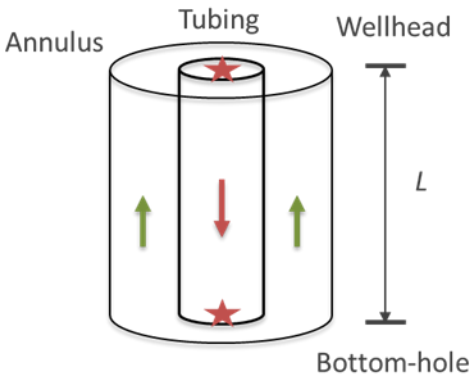

Figure 45- BC in the wellbore.

There might be several combinations of BC; we are presenting the two Dirichlet type BC at the wellhead and bottom-hole, the end of the domain, for predicting the temperature profile as shown in Figure 45. The power fluid is injected continuously into the tubing so that the tubing temperature at the wellhead, T_{twh}, will be the power fluid injection temperature, T_{inj}. The other boundary is the tubing temperature at the near bottom-hole, measured with the Downhole Temperature Sensor (DTS). Here, we assume the measured temperature, $T_{measure}$, is the same with the tubing temperature at the bottom-hole, T_{tbh}, because the DTS installation location in the tubing is just a few feet above the bottom-hole. Summed it up, BC we are presenting here below:

$$T_{twh} = T_{inj}$$
$$T_{tbh} = T_{measure} \tag{A-27}$$

At the bottom-hole, the formation fluid entering the string and injected power fluid are mixing together in the annulus. Using $T_{tbh,}$ we can obtain the T_{abh} from a simple energy balance:

$$w_a C_{p,a} T_{abh} = (w_a - w_t)\, C_{p,prod} T_{eibh} + W_t C_{p,t} T_{tbh} \tag{A-28}$$

Rearranging,

$$T_{abh} = \frac{w_a - w_t}{w_a C_{p,a}} C_{p,prod} T_{eibh} + \frac{w_t}{w_a C_{,pa}} C_{p,t} T_{tbh} \tag{A-29}$$

To obtain constants α and β, we apply the BC simultaneously; we could obtain:

$$\alpha = \frac{(T_{twh} - T_{eiwh} - B_2 g_G)(1 + B_1\lambda_2)e^{L\lambda_2} + (B_1 + B_2 + L)g_G + T_{eiwh} - T_{tbh}}{(1 + B_1\lambda_2)e^{L\lambda_2} - (1 + B_1\lambda_1)e^{L\lambda_1}} \tag{A-30}$$

$$\beta = \frac{(T_{twh} - T_{eiwh} - B_2 g_G)(1 + B_1\lambda_2)e^{L\lambda_1} + (B_1 + B_2 + L)g_G + T_{eiwh} - T_{tbh}}{(1 + B_1\lambda_1)e^{L\lambda_1} - (1 + B_1\lambda_2)e^{L\lambda_2}} \tag{A-31}$$

BC and constants for annulus-injection model

Unlike the previous direction, power fluid is injected into the annulus, it is mixed with the produced hydrocarbon resources at the bottom-hole and then raised up through the tubing. Although the fluid injection point is different, the temperature sensor's installation location is the same as tubing at the bottom-hole depth. Therefore, the BC is the annulus temperature at the wellhead, T_{awh}, and the tubing temperature at the bottom-hole, T_{tbh}.

$$T_{awh} = T_{inj}$$
$$T_{tbh} = T_{measure} \tag{A-32}$$

The injected power fluid is mixed with the produced fluids from the reservoir are mixed in the tubing; the T_{abh} can be obtained from the energy balance following:

$$w_t C_{p,t} T_{tbh} = (w_t - w_a)\, C_{p,prod} T_{eibh} + W_a C_{p,a} T_{abh} \tag{A-33}$$

$$T_{abh} = -\frac{w_t - w_a}{w_a C_{p,a}} C_{p,prod} T_{eibh} + \frac{w_t}{w_a C_{p,a}} C_{p,t} T_{tbh} \tag{A-34}$$

Applying the BC, α, and β can be expressed as:

$$\alpha = \frac{\begin{array}{c} -(T_{awh} - T_{eiwh} + B_1 g_G) e^{L\lambda_2} + (T_{eiwh} - T_{tbh} + B_2 g_G + g_G L) B_1 \lambda_2 \\ -(B_2 + L) g_G - T_{eiwh} + T_{tbh} \end{array}}{(e^{L\lambda_1} - e^{L\lambda_2}) + B_1 \lambda_1 e^{L\lambda_2} - B_1 \lambda_2 e^{L\lambda_1}} \tag{A-35}$$

$$\beta = \frac{\begin{array}{c} (T_{awh} - T_{eiwh} + B_1 g_G) e^{L\lambda_1} - (T_{eiwh} - T_{tbh} + B_2 g_G + g_G L) B_1 \lambda_1 \\ +(B_2 + L) g_G + T_{eiwh} - T_{tbh} \end{array}}{(e^{L\lambda_1} - e^{L\lambda_2}) + B_1 \lambda_1 e^{L\lambda_2} - B_1 \lambda_2 e^{L\lambda_1}} \tag{A-36}$$

APPENDIX B: ANALYTICAL SOLUTION OF HEAT TRANSFER IN THE RESERVOIR

The Steady-state heat transfer model in the reservoir

Recalling Eq. 28, the general energy balance equation for the reservoir system is:

$$\left[\phi s_f \rho_f c_{pf} + \phi s_w \rho_w c_{pw} + (1-\phi)\rho_e c_{pe}\right]\frac{\partial T}{\partial t} + \rho_f u_r c_{pf}\frac{\partial T}{\partial r} + \rho_f u_r \sigma_f \frac{\partial P}{\partial r} +$$

$$\left(\phi s_f \rho_f \sigma_f + \phi s_w \rho_w \sigma_w - 1\right)\frac{\partial P}{\partial t} = \frac{1}{r}\frac{\partial}{\partial r}\left(\lambda r \frac{\partial T}{\partial r}\right) \quad (28)$$

Since it is a steady-state, the first and fourth terms on the left side related to time can be omitted. The organized form of the equation above is:

$$\rho_o u_r c_{po}\frac{\partial T}{\partial r} + \rho_o u_r \sigma_o \frac{\partial P}{\partial r} = \frac{1}{r}\frac{\partial}{\partial r}\left(\lambda r \frac{\partial T}{\partial r}\right) \quad (B\text{-}1)$$

The local fluid velocity u_r can be obtained from Darcy's equation:

$$q = -\frac{kA}{\mu}\frac{\partial p}{\partial r} = -\frac{2\pi r h k}{\mu}\frac{\partial p}{\partial r} \quad (B\text{-}2)$$

$$u_r = \frac{q}{A} = \frac{q}{2\pi r h} = -\frac{k}{\mu}\frac{\partial p}{\partial r} \quad (B\text{-}3)$$

Substituting Eq. (B-2) and (B-3) in the (B-1), then,

$$-\frac{\rho_o q c_{po}}{2\pi r h}\frac{\partial T}{\partial r} - \frac{\mu q^2 \rho_o \sigma_o}{(2\pi r h)^2 k} = \lambda\left(\frac{\partial^2 T}{\partial r^2} + \frac{1}{r}\frac{\partial T}{\partial r}\right) \quad (B\text{-}4)$$

Arranging the Eq. B-2, the second-order ODE form can be following:

$$\frac{d^2 T}{dr^2} + A\frac{1}{r}\frac{dT}{dr} + B\frac{1}{r^2} = 0 \quad (B\text{-}5)$$

The two BCs are (1) the initial temperature at the outer reservoir boundary and (2) an insulated condition at the wellbore wall. The two BCs are following:

$$T(r_e) = T_{ei}$$

$$\left(\frac{\partial T}{\partial r}\right) = 0 \ @\ r = r_w \tag{B-6}$$

The analytical solution of the proposed second-order ODE, which is given as

$$T(r) = T_{ei} + \frac{B r_w^{1-A}\left(r_e^{1-A} - r^{1-A}\right)}{(A-1)^2} + \frac{B}{A-1}\ln\left(\frac{r_e}{r}\right) \tag{B-7}$$

where,

$$A = \left(\frac{2\pi h\lambda + \rho_o q c_{po}}{2\pi h\lambda}\right) \tag{B-8}$$

$$B = \left(\frac{\mu q^2 \rho_o \sigma_o}{(2\pi h)^2 k\lambda}\right) \tag{B-9}$$